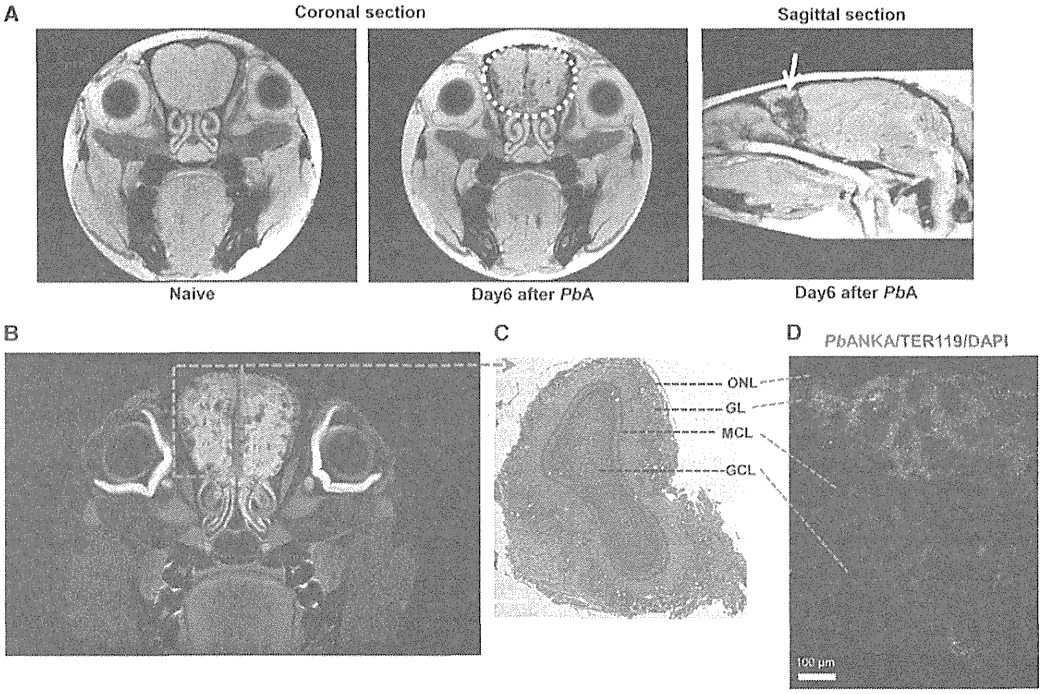

Figure 1. Ultra-High-Field MRI Identifies OLF Bulb as a Vulnerable Location for *Pb*A Parasites

C57BL/6 mice were infected with 10^6 *Pb*A parasites.

(A) 11.7 T MRI of coronal and sagittal sections of mice heads (FLASH T2-star signals, naive v.s. infected). White dotted circle in coronal section and white arrow in sagittal section correspond to OLF bulb.

(B) DWI of coronal section of mouse head on day 6. Gray dotted rectangle and arrow point to HE staining in (C). The images in (A) and (B) are representative of at least five animals.

(C) Histology of coronal section of OLF on day 6 after infection. Hypodense regions correspond to several bleeding sites by HE staining (scale bar, 1 mm). ONL (OLF nerve layer), GL (glomerular layer), MCL (mitral cell layer), GCL (granule cell layer).

(D) IHC of OLF section on day 6. Red, TER119+ erythrocytes; green, GFP-*Pb*A parasites; blue, nuclei (DAPI). Scale bar, 100 μm.

See also Figures S1 and S2.

recent studies have reported CD11c expression on activated CD8 T cells during *Pb*A infection, yet their precise role is not studied well (Tamura et al., 2011). Although these systemic as well as local events for the dysfunction of BBB are well studied, whether the initial brain injury and BBB disruption occur in blood vessels of the whole brain simultaneously or there is a particular location that allows brain to become permissive to iRBC and pathological events has not been fully addressed.

In this study, we investigated the spatiotemporal regulation of pathophysiological and immunological mechanisms of murine CM, using combination of two powerful imaging techniques, an ultra-high-field 11.7 T MRI and multiphoton microscopy (MP). We elucidated the underlying mechanisms where brain became permissive during systemic infection with *Pb*A parasites. We found that the olfactory bulb (OLF), composed of unique capillary structures, serves as a suitable environment for parasites as well as cell migration, and is the first place to sense malaria infection and permit "crosstalk" between the brain and the activated immune system. This links the OLF with loss of smell, high fever, astrocytes, CCL21, CCR7, CXCR3, and CD11c+ CD8 T cells.

RESULTS

Ultra-High-Field MRI Imaging Identifies Olfactory Bulb as Location of Microbleeding in the Brain during ECM

To study changes in mouse brain and visualize ECM-related pathology, we performed ultra-high-field 11.7 T MRI (Mori et al., 2011). Six days after *Pb*A infection when specific ECM symptoms such as disorientation and paralysis begin, 11.7 T MRI displayed dark but clear spots in the bilateral OLF (Figure 1A, coronal section), while no other parts of the brain, including cerebrum or cerebellum, showed such spots (Figure 1A, sagittal section). When diffusion-weighted images (DWI) were obtained, details of the OLF region were more evident and remarkably similar to the histological details, where hypodense regions correspond to the bleedings by hematoxylin and eosin (H&E) staining (Figures 1B and 1C). Immunohistochemistry (IHC) also confirmed that bleeding (TER119+ erythrocytes) and GFP-*Pb*A parasites were present in the same area of OLF and were as deep as the granular cell layer (GCL) (Figure 1D). Additional MRI at earlier time points did not detect changes earlier than day 6 postinfection (see Figure S1B available online). Furthermore, several MRI images after the onset of symptoms showed

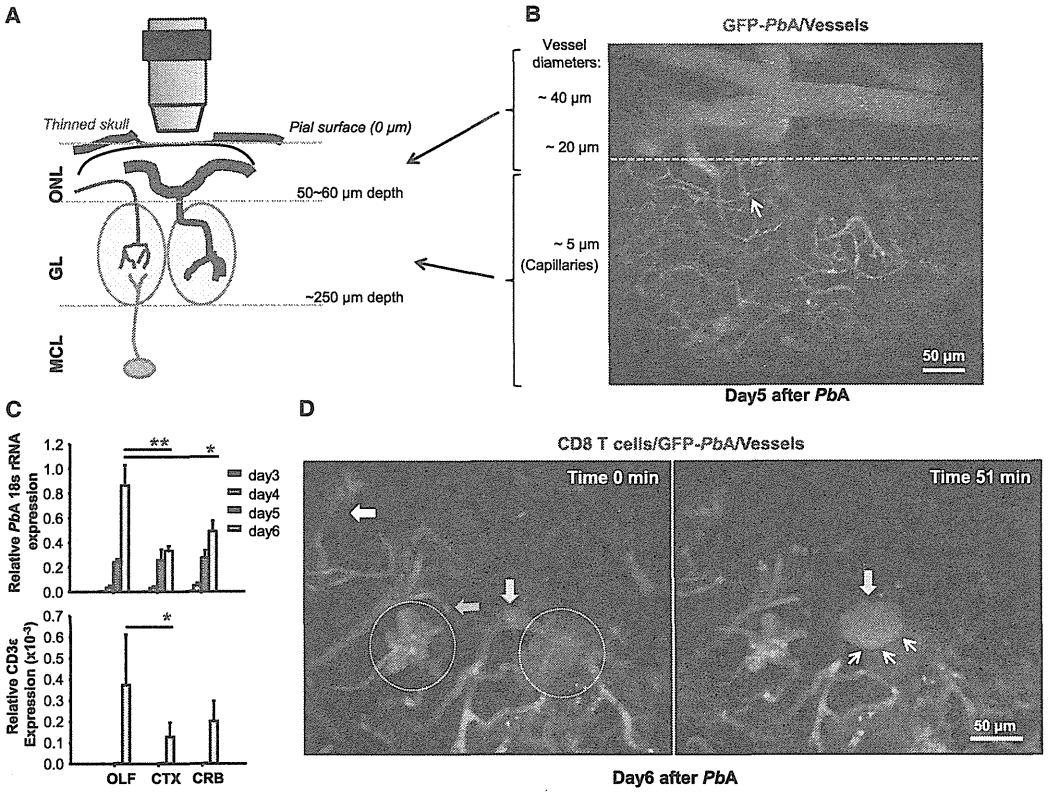

Figure 2. Intravital Multiphoton Imaging of OLF Bulb during Infection

(A) Schematic representation of MP microscopy through the thinned-skull of dorsal OLF bulb. The depth of the images is ~150 μm from the pial surface in which capillaries (red, diameter <5 μm) in the GL are visualized. Larger vessels (surface arteries and arterioles, diameter ~20–40 μm) are located in the ONL.

(B) A representative snapshot intravital MP image from WT mouse OLF bulb on day 5 after GFP-*Pb*A infection, related to Movie S1. White arrow shows GFP parasites attached/occluded to the blood vessel labeled with red TRITC-Dextran. Gray line separates bigger vessels and capillaries. Scale bar, 50 μm.

(C) *Pb*A parasite load and CD3ε (pan-T cell surface marker) were quantified by qPCR using primers specific for *Pb*A 18S rRNA and CD3ε on days 3, 4, 5, and 6 after infection in the OLF, cortex, and cerebellum. Results are presented as relative mRNA units (mean ± SE, n = 3 for days 3, 4, and 5 and n = 8 for day 6). *$p < 0.05$ and **$p < 0.01$ for infected versus noninfected mice by Mann-Whitney test.

(D) Fresh microbleeding in OLF. Representative snapshot images (0 and 51 min time point) on day 6 after infection, related to Movie S2. Red, vessels (red TRITC-Dextran); green, GFP-*Pb*A (green arrow); blue, CD8 T cells (anti-CD8 Ab, white arrow). Red areas in gray circles show already-bled regions, yellow arrows show the angular vessels where fresh bleeding will occur, and white arrows show leaked blood vessel indicating fresh bleeding occurred, on the right image.

See also Movie S1, Movie S2, Movie S3, and Movie S4.

different degrees of hemorrhages in the OLF, perhaps implying progressive disease symptoms (Figure S2). However, there was no clear evidence of microhemorrhages in other parts of the brain, even the heavy bleeding occurred in OLF (Figure S2). Furthermore, mice infected with lethal parasites, *P. yoelii*L (*Py*L), had no microbleedings in their OLF (Figure S3A). It is therefore reasonable that our ultra-high-field MRI setting enabled the identification of OLF as a vulnerable area during *Pb*A infection, where bleedings could easily occur compared with other parts of the brain.

Intravital Multiphoton Imaging of Parasites within OLF Trabecular Small Vessels

We next investigated why and how bleedings occur, including possible involvement of the BBB disintegration, from the OLF during ECM. The OLF is composed of trabecular small vessel structures, which are high in density and oriented in different directions (radially and tangentially). These complex vessels, together with neuron and glial cells, make synaptic interactions in glomeruli and may serve as a scaffold environment for neuronal cell migration in the tissue (Bovetti et al., 2007; Danielyan et al., 2009). To examine whether this unique vessel architecture could be a "weak spot" for iRBC and infection-related events, OLF was visualized by intravital MP microscopy. MP imaging of rodent OLF bulb has previously been performed as deep as GL (~150 μm) which are rich in capillaries (Figure 2A) (Chaigneau et al., 2003; Petzold et al., 2008; Sawada et al., 2011). We performed thinned-skull surgery over the dorsal OLF bulb to maintain tissue intact (Sawada et al., 2011). Live images of OLF vessels showed this region has anatomically complex capillary architecture (diameter <5 μm) (Petzold et al., 2008) and is suitable for the adhesion/occlusion of circulating iRBC, shown as GFP signals expressed in *Pb*A parasites, 5 days after infection (Figure 2B; Movie S1). As seen in Movie S1, the speed

of some GFP-labeled parasites was reduced and/or stopped, eventually causing occlusion. This was in accordance with a significantly higher parasite load as well as T cells' accumulation in the OLF (Figure 2C). Taken together, these results suggest that OLF is a unique area for ECM pathogenesis, possibly due to its complex capillary architecture, whereby circulating iRBCs may slow down, attach, and/or become sequestered, ultimately leading to bleeding.

CD8 T Cells Traffic via the Blood Vessels in OLF

Intravascular accumulation of CD8 T cells in the brain was shown to have an important role in the pathogenesis of ECM (Miyakoda et al., 2008). We examined if CD8 T cells could be observed and/or related to microbleeding by intravital MP imaging. Live MP imaging of labeled CD8 T cells and GFP-*Pb*A parasites in OLF clearly demonstrated that microbleeding occurred at the branching capillaries (Figure 2D; Movie S2). As seen in Movie S2, red dextran-labeled capillary structures were altered (red dye almost leaked into tissue). Importantly, CD8 T cells were increased in numbers and "crawling" back and forth in the vessels during the development of ECM (Figure 2D; Movie S2, Movie S3, and Movie S4), and some were associated around the bled regions (Movie S2). Those CD8 T cells in the OLF could be passively moving during unstable blood flow in the terminal phase of ECM; however, our constructed 3D movie in the relatively larger vessels (around 10 μm) clearly indicated that CD8 T cells attached vessels and actively crawling along the vessel wall (Movie S3). These crawling behaviors of T cells were not due to in vivo anti-TCRβ or anti-CD8 antibody labeling in which the same antibody had no effect on T cells of naive mice (Movie S4; data not shown). Rather, activated T cells accumulated in the OLF capillaries starting day 5 and highly increased in numbers with crawling behaviors (Movie S4). Together, these live OLF images indicate that accumulated iRBC with increased and crawling CD8 T cells might leak out of the vessel via microbleeding of the OLF capillaries.

Olfactory Function Is Destroyed during ECM

Given the above findings that microbleeding occurs in OLF during ECM, we hypothesized that the OLF function (smell) would be affected, because OLF contains OLF nerves that form a complex physiological synapse for odors. To assess OLF function, we performed a simple buried food test (BFT) (Yang and Crawley, 2009). OLF function was significantly impaired as early as day 4 after infection, as determined by the delayed time to find buried food (Figure 3A), compared with mice that are resistant to ECM such as BALB/c or *Rag2*$^{-/-}$ mice or mice infected with lethal *Py*L parasites (Figure 3B). Thus, olfaction loss might allow the prediction of manifestations of ECM such as bleeding in the OLF and potential loss of BBB integrity.

To evaluate whether the olfaction loss directly correlated with the loss of BBB integrity, Evans-blue dye was injected into mice at early time points (days 3–6) after infection and blue dye extravasation into brain tissues were monitored. In accordance with MP imaging observations where iRBC slowed down and stopped in the vessels, blue dye extravasation into tissue appeared from the OLF as early as day 5 after infection, while the whole brain was blue on day 6 or 7 (Figure 3C). The BBB is restrictive due to tight junctions (TJs), and proteins such as zonula occludens-1 (ZO-1) and ZO-1 were indicated to be localized in the OLF epithelium, OLF sensory neurons, and OLF bulb MCL (Miragall et al., 1994). On day 6 after infection, significant discontinuation of ZO-1 was observed in the MCL, which coincided with the accumulation of GFP-*Pb*A parasites (iRBC) (Figure 3D), suggesting that altered ZO-1 expression in TJ of OLF might be associated with the loss of BBB integrity during ECM.

High Fever and Chemokine Storm during ECM Are Associated with OLF Dysfunction and Physical Damage

We next sought possible factors that contributed to OLF dysfunction during ECM. High fever was shown to be one of the facilitating factors for the BBB loss (Kiyatkin and Sharma, 2009). Because high fever is an important symptom of malarial coma, we developed a thermal camera system that allowed continuous and noninvasive measurement of mouse body temperature. The body temperature of infected mice revealed that high-fever attacks begin 24 hr before the onset of ECM symptoms (around day 5) and continue for 24 hr, then end with thermal loss and death in the following 12–24 hr (Figure 3E; Movie S5). When *Rag2*$^{-/-}$ mice, T/B cell-deficient mice that do not develop ECM, were infected, no sign of high fever throughout the infection was observed, and the OLF was intact by MRI (Figures 3F and S3B). Moreover, mice infected with *Py*L or *P. yoelii*NL had no fever (Figures 3G and S4A), suggesting that the fever could be *Pb*A specific. Although the precise mechanism by which high fever triggers and/or facilitates BBB disintegration followed by OLF dysfunction and bleeding is not clear, the data suggest that high fever occurs 24 hr before ECM-related death and may be correlated to BBB leakage. Of note, elevated systemic serum cytokine levels at day 5 after infection may support the notion that cytokine storm accompanies high fever (Figure S4B).

CCL21 Is Expressed in OLF at the Early Stage of Infection

We further investigated other possible factors relevant to olfaction loss. Chemokines are early mediators of inflammation and have increasingly being recognized as contributors in the pathogenesis of fever (Machado et al., 2007). As some chemokines and cytokines have critical roles in the development of ECM, expression levels of several of them were measured in the OLF. CCL21 and CCL19 mRNA and protein levels were highly expressed as early as day 3 after infection in the OLF bulb (Figures 4A and 4B), suggesting the early expression of chemokines, especially CCL21, might be important during ECM.

These results above prompted us to examine whether CCR7 (receptor for CCL21 and CCL19) is involved in the pathology of ECM. We infected WT and littermate *Ccr7*$^{+/-}$ and *Ccr7*$^{-/-}$ mice with *Pb*A and followed their survival. A significant increase in survival among *Ccr7*$^{-/-}$ mice occurred, and death was caused by high parasitemia, with no difference in parasite levels between groups during ECM period (Figure 4C; data not shown). To evaluate whether olfaction in *Ccr7*$^{-/-}$ mice was intact, a BFT was performed and found to be intact (Figure 4D). Interestingly, high fever occurred with a delayed onset in *Ccr7*$^{-/-}$ mice (~48 hr) (Figure 4E) with no signs of bleeding in the OLF at day 6 (Figures S5A and S5B). Evans blue staining gradually occurred about 80% of *Ccr7*$^{-/-}$ mice brains onward of day 8 (Figure S5B). These data suggested that CCR7 has a role in the pathogenesis

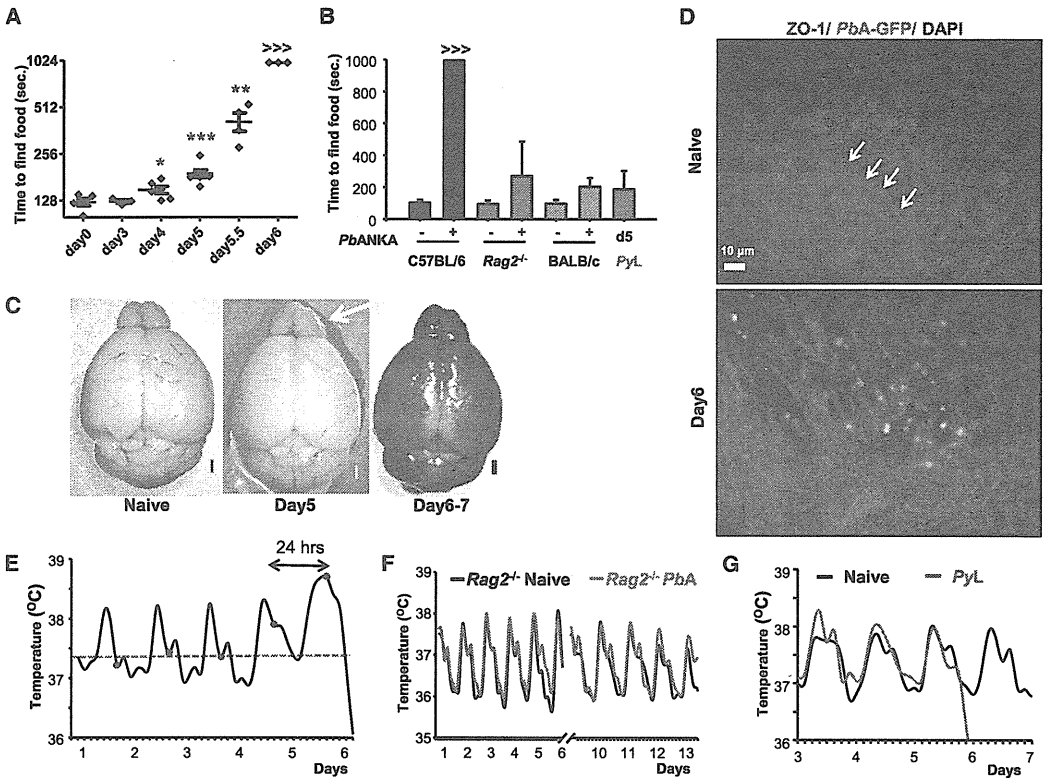

Figure 3. Olfaction Loss and Fever Occur during ECM

(A) To assess OLF function, mice were subjected to BFT at the indicated time points. The delay in time to find food is shown in seconds (mean ± SD, n = 4–6 per time point). *p < 0.05, **p < 0.01 and ***p < 0.001 by Student's t test or Mann-Whitney test.

(B) OLF function of naive and *Pb*A- or *Py*L-infected C57BL/6, *Rag2*$^{-/-}$, and BALB/c mice assessed by BFT on day 6 after infection (time to find food is shown in seconds, mean ± SD, n = 5–8 per group). No statistical significance observed between groups by Student's t test. >>> in (A) and (B) shows time greater than 900 s.

(C) Evans blue dye was injected i.v. to assess BBB leakage in naive or infected mice at the indicated time points. Two hours after dye injection, mice were sacrificed, the brains removed, and images captured by dissecting microscopy. White arrow, OLF bulb (scale bar, 1 mm).

(D) IHC of OLF bulbs at the indicated time points. Red, TJ protein ZO-1; green, GFP-*Pb*A; blue, nuclei (DAPI). White arrows show the continuous line of ZO-1 protein around the MCL in naive mice (scale bar, 10 µm).

(E) Thermal camera monitoring of infected C57BL/6 mice, related to Movie S5. Mice movements and fever were continuously recorded in the cages. Mean fever measurements were calculated every 3 hr. Dotted green line shows the median fever level of the same mouse before infection. Red dots show 0–3 a.m. time points for each day.

(F and G) Fever in *Pb*A-infected *Rag2*$^{-/-}$ mice (F) and *Py*L-infected C57BL/6 mice (G) were recorded by thermal camera monitor. Mean fever measurements were calculated every 3 hr.

The data presented in (E)–(G) are representative of at least three infected mice per group. See also Figures S3 and S4.

of ECM, contributing to OLF dysfunction, microbleeding, and high fever.

CCR7 Expression Is Critical for CD8α DC Priming of CD11c+ CD8 T Cells but Not for Their Migration into Brain

We next investigated underlying mechanism responsible for the increased survival of *Ccr7*$^{-/-}$ mice from ECM. Since CCR7 is important in the migration of immune cells such as DCs and T cells to the secondary lymphoid organs, we examined the recruitment of T cells in the brain. Flow cytometric analysis of immune cells obtained from brains 6 days after infection showed that CD8 T cell accumulation was decreased by 50% in *Ccr7*$^{-/-}$ mice (Figure 5A). A recent report suggested that among the CD8 T cells recruited into the brain, CD11c+ CD8 T cells were highly activated and possibly involved in the pathogenesis by producing IFN-γ and granzyme-B (Tamura et al., 2011). Consistent with this report, we found that CD8 T cells in the brain of infected mice were mostly CD11c+, a population that were remarkably reduced in the infected brains as well as spleens of *Ccr7*$^{-/-}$ mice by percentage, numbers, and activity (Figures 5A, 5B, and 5C, respectively) and secreted IFN-γ (Figure 5D).

We further evaluated whether decreased percentages of CD11c+ CD8 T cells in *Ccr7*$^{-/-}$ mice were caused by defects in the prior priming in spleen. It has been suggested that CD8α+ DCs predispose CD8 T cells in the pathogenesis of ECM, as they can cross prime CD8 T cell responses (Lundie et al., 2008; Piva et al., 2012). We confirmed by infecting basic leucine zipper transcriptional factor ATF-like 3 (*Batf3*)-deficient mice which lack CD8α DCs in the spleen (Murphy et al., 2013)

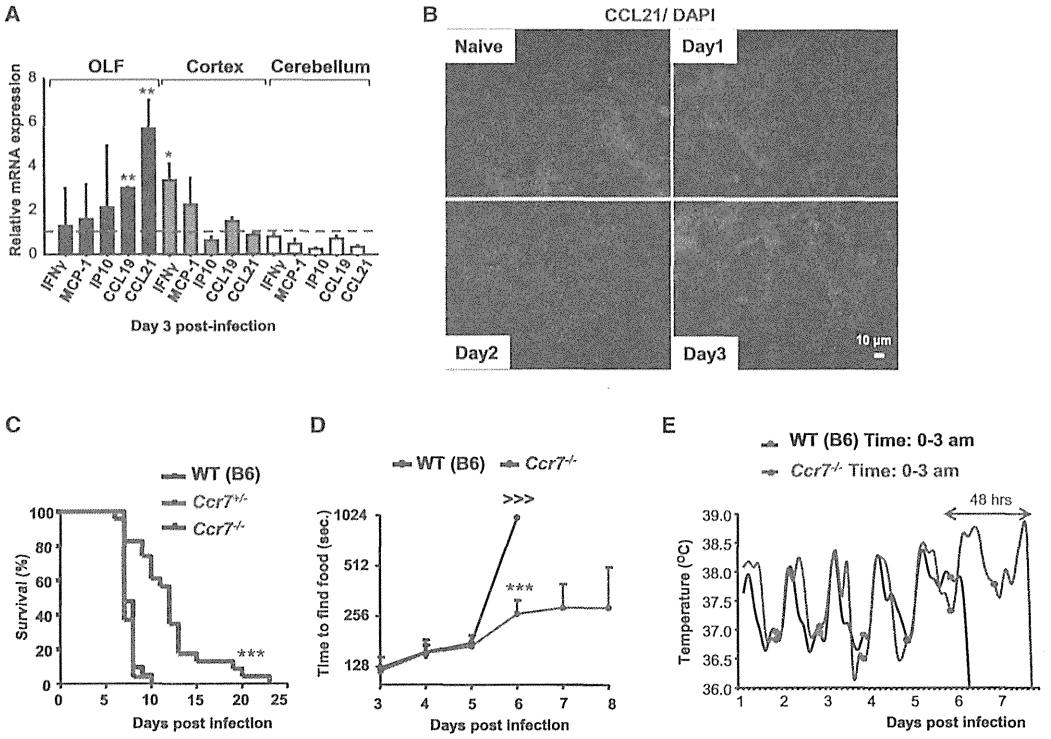

Figure 4. CCL21 Activity Occurs at OLF Bulb during Infection

(A) Brain tissues (OLF bulb-cortex-cerebellum) were removed on day 3 postinfection. Expression of indicated chemokine/cytokine mRNA was analyzed by real-time qPCR. Results (mean ± SD) are presented as fold induction compared to naive mice relative mRNA units ($n = 3$). Red dotted line corresponds to 1. $^*p < 0.05$, $^{**}p < 0.01$, infected versus noninfected mice by Student's t test.

(B) IHC of OLF bulb sections from infected mice (on days 0–3 postinfection). Red, CCL21; blue, nuclei (DAPI) (scale bar, 10 μm).

(C) Survival curves of WT (C57BL/6, $n = 21$), *Ccr7*$^{+/-}$ ($n = 27$) and *Ccr*$^{-/-}$ ($n = 23$) mice after infection with 10^6 *Pb*A. $^{***}p = 0.0004$, log rank (Mantel-Cox) test.

(D) Infected WT and *Ccr7*$^{-/-}$ mice were subjected to BFT. The time to find food is shown in seconds (mean ± SD, $n = 4$ per time point). $^{***}p < 0.001$ by Student's t test. >>> shows time was greater than 900 s.

(E) Continuous fever monitoring of infected WT and *Ccr7*$^{-/-}$ mice. Mean fever measurements were calculated for every 3 hr. Blue and red dots show 0–3 a.m. time points for each day. The data presented are representative of at least three infected animals per group.

See also Figure S5.

that the number of activated CD11c+ CD8 T cells in spleen and their accumulation in brain was significantly impaired in *Batf3*$^{-/-}$ mice with improved survival rate compared to controls (Figures S6A–S6C). However, *Ccr7*$^{-/-}$ mice had almost comparable numbers of CD8α DCs in spleen (Figure S6A); we therefore designed experiments to understand if functional CCR7 expression on CD8α DCs is required for CD8 T cell activation.

Functional CCR7 Is Required for CD8α DCs' Priming of CD11c+ CD8 T Cells

To seek the role of CCR7 expression on CD8α DC, we purified CD8α DCs from infected *Rag2*$^{-/-}$ mice with intact DCs but no T/B cells (McLellan et al., 2002). Splenic CD8α+ DCs, but not CD8α- DCs, from *Rag2*$^{-/-}$ mice expressed high levels of CCR7 at day 5 after infection (Figure S7A). These CCR7+ CD8α+ DCs were purified (Figure S7B) and adoptively transferred to *Ccr7*$^{-/-}$ mice in which efficiently restored the recruitment of activated CD11c+ CD8 T cells (which originated from *Ccr7*$^{-/-}$ mice) in the brain and accelerated ECM (Figure 5E). Together, these findings suggest that functional CCR7 expression on activated CD8α+ DCs has a critical role in the pathogenesis of ECM, possibly by activating CD11c+ CD8 T cells and their expansion. However, CCR7 expression on CD11c+ CD8 T cells is dispensable for the migration of these cells.

CCL21 Expressed in OLF Coincides with Activation of Astrocytes and May Be Important for the OLF Migration of CD11c+ CD8 T Cells

The finding that CCR7 is dispensable for the OLF migration of CD11c+ CD8 T cells has implied the importance of CCL21 during priming of CD8 T cells. On the other hand, as CCL21 expression was also observed in OLF from day 3 of infection, we evaluated the possibility that CCL21 might have an additional role on the recruitment of CD8 T cells via an alternative chemokine receptor interaction other than CCR7. Thus, we further analyzed the localization and/or source of CCL21 in the infected OLF. Although it was difficult to address the cell type expressing CCL21, CCL21 staining was confined to the endothelium of inflamed blood vessels where astrocytes are often colocalized (Figure 6A). Astrocytes are specialized cells guarding and sensing blood

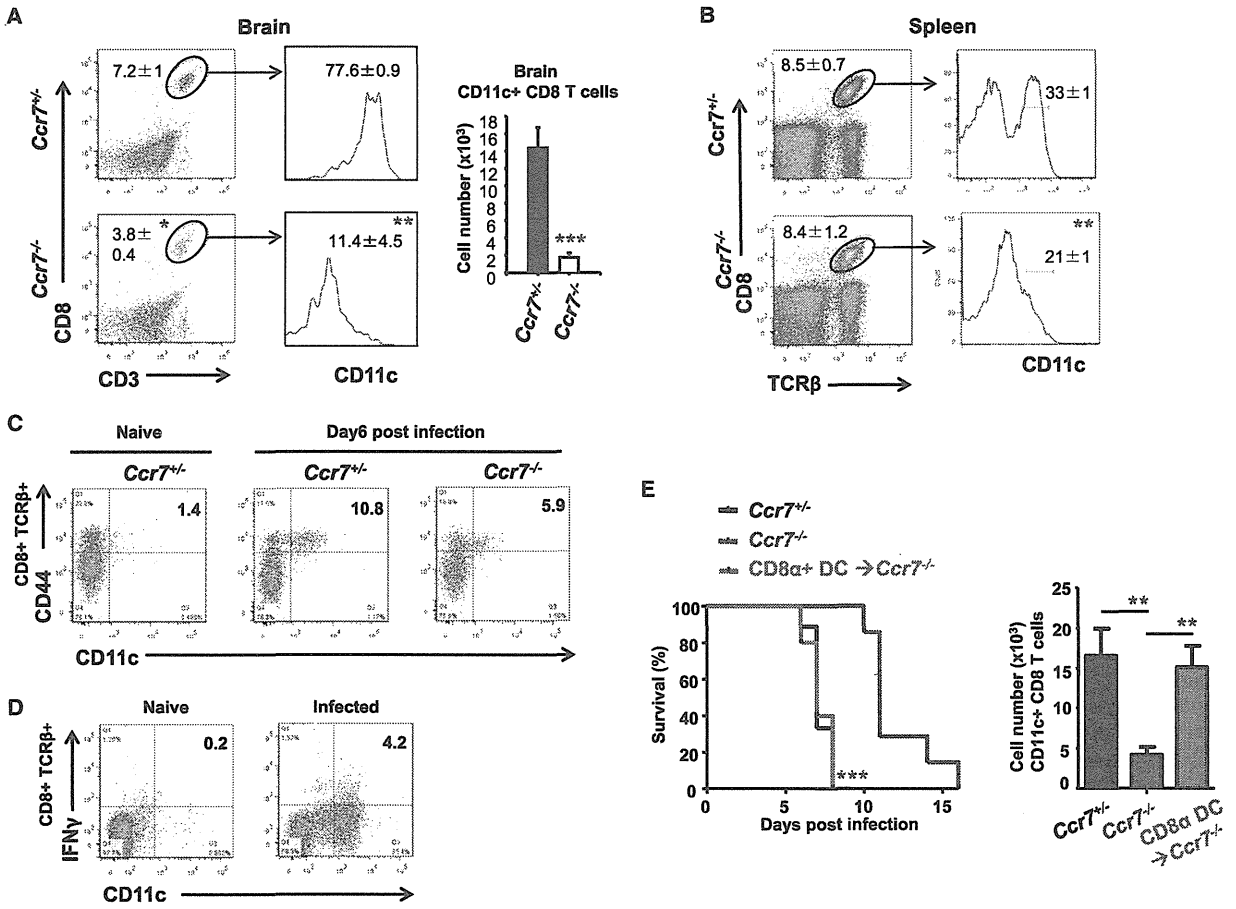

Figure 5. CCR7 Expression Is Critical for CD8α DC Priming of CD11c+ CD8 T Cells but Not for Their Migration into Brain

WT and *Ccr7*$^{-/-}$ mice were infected.

(A and B) Flow cytometric analysis of whole brain (A) and spleen (B) cells on day 6 postinfection. Numbers in the insets show percentages of CD8 T cells and their CD11c expression, and the right figure in (A) shows absolute numbers of CD11c+ CD8 T cells in brain (mean ± SEM of four to eight mice per group. *$p < 0.05$, **$p < 0.01$, and ***$p < 0.001$ infected *Ccr7*$^{-/-}$ versus infected *Ccr7*$^{+/-}$ mice by Mann-Whitney test).

(C) Activation status of CD11c+ CD8 T cells in spleen of WT and *Ccr7*$^{-/-}$ mice was determined by CD44 surface staining.

(D) Intracellular staining of IFN-γ secreting CD11c+ CD8 T cells in spleens of WT mice.

(E) Enriched CD8α DCs from infected *Rag2*$^{-/-}$ spleens were adoptively transferred to *Ccr7*$^{-/-}$ mice and infected with *Pb*A, and survival was monitored. Survival curves of *Ccr7*$^{+/-}$ (n = 9), *Ccr7*$^{-/-}$ (n = 7), and transferred *Ccr7*$^{-/-}$ (n = 5) mice after infection are shown. ***$p = 0.0005$, *Ccr7*$^{-/-}$ versus CD8α DC transferred *Ccr7*$^{-/-}$ mice by log rank (Mantel-Cox) test. FACS analysis shows the numbers of accumulated CD11c+ CD8 T cells in brains (mean ± SD of three mice per group). **$p < 0.01$, infected *Ccr7*$^{+/-}$ versus infected *Ccr7*$^{-/-}$ mice and *Ccr7*$^{-/-}$ versus infected CD8α DC transferred *Ccr7*$^{-/-}$ mice by Student's t test.

See also Figures S6 and S7.

vessel changes via their endfeet, and their redistribution in retina was implicated during ECM (Medana et al., 1996). On day 6 after infection, morphological alterations of the astrocytes such as ill-spaced distribution and thick and longer processes were evident in OLF (Figure 6B). Moreover, astrocyte interaction with PECAM-1 was greatly altered. Interestingly, CCL21 staining, especially with its fiber-like structures, was in close interaction with CD8 T cells in the OLF (Figure 6C). Given that CXCR3 has promiscuous interaction with several chemokines including CCL21 especially in microglia and astrocytes (Rappert et al., 2002; van Weering et al., 2010) and is a critical molecule for CD8 T cell migration during ECM (Campanella et al., 2008; Hansen et al., 2007; Van den Steen et al., 2008), to understand if there is a chemotactic interaction between CCL21- and CXCR3-expressing CD11c+ CD8 T cells, we performed in vitro transwell migration assay. The CXCR3+ CD11c+ CD8 T cells dose-dependently migrated toward CCL21 (Figure 6D), suggesting CCL21 may be involved in the recruitment of these cells into OLF during ECM.

Blocking CCR7-CCL21-CXCR3 Axis Is a Potential Intervention for ECM

Given that CCR7-CCL21 and CCL21-CXCR3 axis may have roles in ECM immunopathology, we evaluated whether CCL21

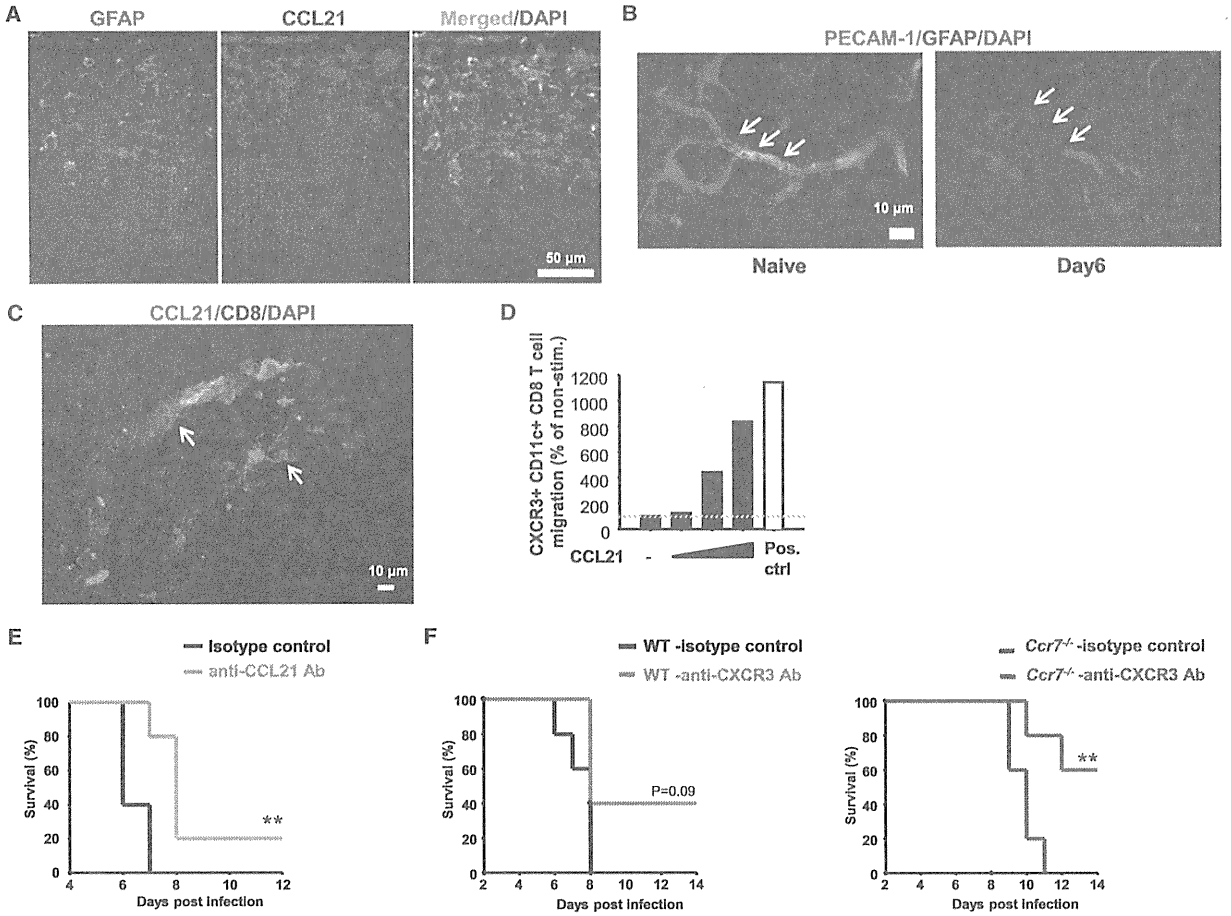

Figure 6. CCL21 Expressed in OLF Coincides with Astrocyte Activation and May Be Involved in the Migration of CD11c+ CD8 T Cells

(A) IHC of OLF bulb sections from infected mice on day 6. Green, astrocytes (GFAP); red, CCL21; blue, nuclei (DAPI) (scale bar, 50 μm).

(B) Astrocyte endfeet wrap blood vessels in GL. IHC of OLF bulb GL sections. Green, vessels (PECAM-1); red, astrocytes (GFAP); blue, nuclei (DAPI). White arrows, blood vessels (scale bar, 10 μm).

(C) CD8 T cells associate with CCL21 in OLF. IHC of OLF bulb sections. Green, CCL21; red, CD8 T cells (CD8); blue, nuclei (DAPI) (scale bar, 10 μm). White arrows show fiber-like structures of CCL21 interacting with CD8 T cells.

(D) Migration of purified splenic CD11c+ CXCR3+ CD8 T cells from infected mice in response to recombinant CCL21 (0–2 μg/ml). Human SDF1-α (80 ng/ml) was used as positive control. The migrated cells were counted by flow cytometer, and chemokine-induced migration was normalized to the unstimulated control (gray dotted line) and depicted as percentage.

(E) Mice were i.v. injected daily from the day of infection (0–3 days) with recombinant mouse anti-CCL21 Ab (50 μg per day) and isotype control, and survival was monitored (n = 5 per group, $^{**}p < 0.01$, log rank [Mantel-Cox] test).

(F) Survival curves of recombinant anti-CXCR3 and isotype control antibody treated groups of WT and *Ccr7*$^{-/-}$ mice after infection. Mice were i.v. injected with antibodies twice at 100 μg per day per mouse on days 4 and 5 after infection. p = 0.09 for isotype control versus anti-CXCR3 Ab group, and $^{**}p < 0.01$ for *Ccr7*$^{-/-}$ isotype control versus *Ccr7*$^{-/-}$ anti-CXCR3 Ab group by log rank (Mantel-Cox) test (n = 5 per group).

could be exploited as a therapeutic target for the intervention of ECM. Treatment of mice with i.v. anti-CCL21 Ab for the first 3 days of infection led to significantly better survival compared to isotype-control treated mice (Figure 6E). However, anti-CCL21 Ab treatment from day 4 after infection did not have a profound effect on ECM progression (data not shown), suggesting involvement of CCL21 during late stage of ECM might be compromised by the activation of other effector mechanisms. Therefore, we performed combined targeting of CCL21 and CXCR3 by using *Ccr7*$^{-/-}$ mice. Blocking CXCR3 by suboptimal doses of anti-CXCR3 Ab on days 4 and 5 after infection led to significant survival from ECM in *Ccr7*$^{-/-}$ mice as compared to controls (Figure 6F). These data have revealed a proof of concept that combinational blocking of chemokines could be a therapeutic intervention for ECM.

DISCUSSION

Although brain is severely dysfunctional during ECM due to multiple pathological events such as BBB disruption, vascular

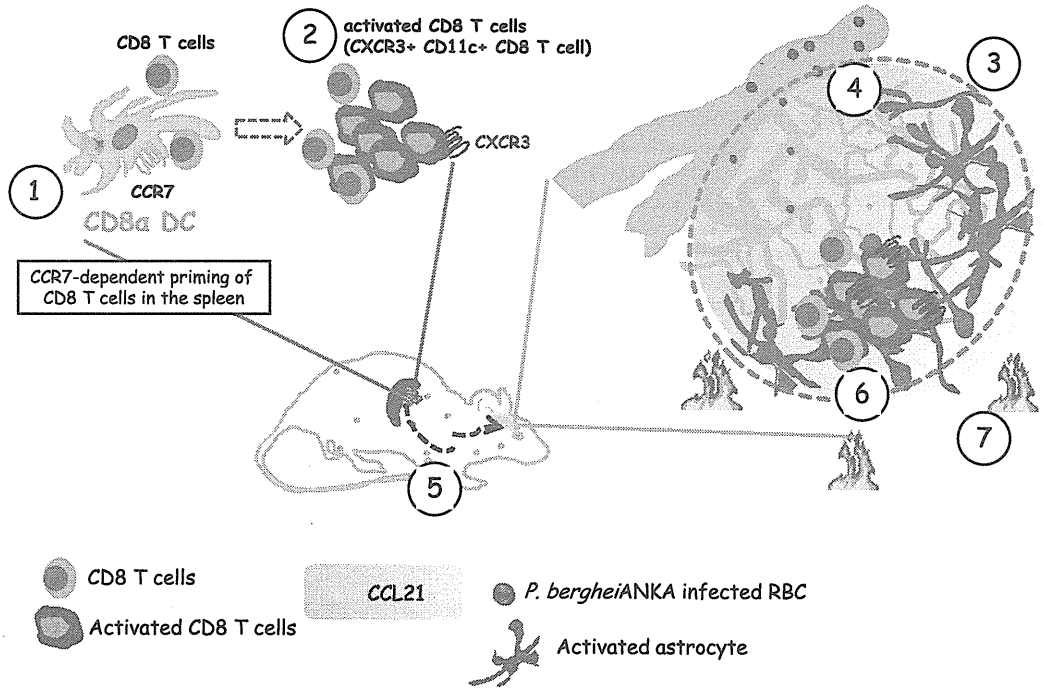

Figure 7. OLF Bulb Could Be a "Gateway" for *Plasmodium*-Infected Erythrocytes' Accumulation in the Brain

Once host is infected with *Pb*A parasites, immune cells are activated in periphery such as blood and spleen. Infection-activated CD8α+ DCs in spleen (1) gain ability to crossprime antigens to CD8 T cells via the expression of CCR7. Some of the activated CD8 T cells become effector phenotype by expressing CD11c and CXCR3 (2). These activated immune cells, iRBC, or parasite products are sensed by astrocytes and their surrounding endfeet around the vessels in the OLF glomeruli (3) which possibly induce CCL21 secretion from astrocytes (4), and having a part in opening the BBB gateway to immune cells. Activated CD8 T cells migrate specifically to OLF bulb, where CCL21 and various other effector molecules are secreted (5 and 6), leading to fever and bleeding at OLF (7).

leakage, and immune cell accumulation (especially CD8 T cell infiltration), the exact location at and method by which brain is disrupted are poorly understood. In the current study, we have identified in mice that the OLF region is a vulnerable location for vascular leakage during ECM in which this discovery could only be possible by using an ultra-high-field MRI in combination with MP live imaging microscopy. We further identified that there is an early symptom, olfaction loss, before the onset of coma. Given that even 1 day early detection of malarial coma could increase treatment success dramatically, this previously unnoticed, truly overlooked location and detection of olfaction loss during malaria infection may provide early, cheap, and easy diagnosis of ECM. In search for the underlying mechanism(s) of pathology of ECM via OLF, we found that CCL21 possibly secreted from OLF astrocytes might have a role for the recruitment of pathological CD11c+ CD8 T cells into brain (Figure 7). We further extended this potential function of CCL21 into a therapeutic strategy by blocking chemokine-receptor interactions when the early symptom of ECM, olfaction loss, was evident.

An interesting question is why is the OLF bulb the first place affected by *Plasmodium* parasites? The OLF is composed of very dense capillaries oriented in different directions (radially and tangentially) that exhibit a network of TJ with the thin astrocyte endfeet surrounding the vessel, creating a BBB "guardian." This restricts the flux of substances between the blood and neuronal tissue, maybe via the TJ's capability to transmit information between astrocytes (Chen et al., 2013; Whitman et al., 2009). In the current study, the ONL, blood vessel scaffold around the GL and as deep as MCL was targeted by iRBC or parasite-related events. At present, we do not know what parasite or related factors might contribute to this; however, the TJ network (e.g., ZO-1) might be targeted and possibly disintegrated during ECM. It is possible that perivascular astrocyte endfeet, which are rich in GL and MCL, sense changes in the vessels (De Saint Jan and Westbrook, 2005; Petzold et al., 2008), even when the peripheral parasite burden was very low. Previous studies have reported in cortex that postcapillary venules (labeled with anti-CD14) and/or arteriolar vasoconstriction play a dominant role in ECM pathogenesis (Cabrales et al., 2010; Nacer et al., 2012). Although PECAM-1 staining of OLF vessels seem to be altered in our study, whether there is a differential role for different anatomical vessel structures of OLF needs to be further investigated.

The OLF bulb is known as a dynamic location for OLF nerve projections, especially chemosensations. OLF nerves initiate from the nasal mucosa and terminate in the OLF bulb through the cribriform plate. Lymphatic and blood vessels surround these nerves through which molecules, cells and even pathogens can gain access to brain parenchyma (Danielyan et al., 2009). Recent studies revealed that neuronal cells from the

central nervous system (CNS) migrate via nerves and along brain blood vessels toward the OLF bulb (Bovetti et al., 2007), suggesting that OLF could be a dynamic cell migration gateway between the external environment and CNS. Therefore, it is reasonable that patients suffering from neurodegenerative Alzheimer's or Parkinson's disease and autoimmune diseases experience OLF dysfunction as an early symptom (Mesholam et al., 1998; Strous and Shoenfeld, 2006). Similarly, our findings imply that these dense and directionally structured blood capillaries could also be a suitable environment for *Plasmodium* parasites' adhesion/occlusion—even though iRBC migrate inside the vessels—and these consecutive events could be a reason for olfaction loss.

This study identified factors that might be involved in preceding the BBB opening from the OLF bulb. One of the factors involved in BBB leakage might be a high fever. Although it is speculated that there should be thermoregulation in mouse models of malaria similar to murine sepsis models, currently there have been no reports of a febrile response in mouse malarias (Lamb et al., 2006). Moreover, ECM, in contrast to human infection, is considered to cause hypothermia. By using a thermal camera, a relatively simple technology developed recently (T.A. and K.J.I., unpublished data), we detected a distinct fever period occurring 24 hr before the final manifestation of disease, thermal loss, and death. Importantly, the fever period correlated with severe olfaction loss. Given that the circadian rhythm of mice prevents accurate fever measurement at a single time point, it is not surprising that previous studies could only measure final thermal loss at the final stage of disease. We concluded that systemic and local cytokine/chemokine storm might cause high fever in mice, similar to human CM cases, and probably had the major role in the loss of BBB integrity. Importantly, lack of high fever in *Rag2*$^{-/-}$ mice and in lethal and nonlethal *Py* infections may confirm that fever is associated with ECM and might be related to BBB leakage. However, the mediators causing fever during ECM and their direct role on BBB disruption are currently unknown. The scientific understanding of the mechanism of fever and its relation to cytokinesis have only been performed by using bacterial products such as LPS and LPS challenge models in which fever is known to correlate well with the cytokines IL-1β and TNF-α (Netea et al., 2000). In contrast, there is a lack of information and direct correlation in murine malaria that these very same cytokines would be elevated and cause malarial fever. Clearly, this area needs further investigation.

Astrocytes are common CNS-residing cells essential for regulating blood flow and maintaining the BBB. Astrocytes are also important in immune defense of the CNS by expressing a wide variety of chemokines during physiological and pathological conditions (de Haas et al., 2007; Medana et al., 1996). Furthermore, astrocytes increase CCL21 expression in response to CNS injury and infection (Lalor and Segal, 2010; Noor et al., 2010). An increased CCL21 expression in the OLF, specifically in GL where high numbers of astrocytes are present, led us to study *Ccr7*$^{-/-}$ mice, because CCR7 regulates CNS lymphocyte trafficking via interactions with its ligands, CCL19 and CCL21 (Noor and Wilson, 2012). In addition, previous studies identified chemokine receptors such as CCR5 and CXCR3 that might be important for cellular migration into the brain (Belnoue et al., 2003a, 2003b; Miu et al., 2008). Although the role of CCR7 in the induction and maintenance of antiviral effector and memory CTL responses was extensively examined (Junt et al., 2004), the role of CCR7 during a severe malaria model such as ECM was not investigated before. We found that expansion and migration of effector CD11c+ CD8 T cells were severely impaired in the absence of CCR7 in spleen as well as brain. However, our detailed analysis with CD8α DCs from *Rag2*$^{-/-}$ mice led to the conclusion that the expansion of CD11c+ CD8 T cells required an antigenic stimulus from CD8α DCs in spleen and the presence of CCR7. However, given that *Batf3*$^{-/-}$ mice could escape from ECM only partially (~50%), whether compensation occur between members of the BATF family in DC development as a result of the combined actions of BATF3, BATF, and BATF2 or compensation occurs between other DC types during ECM, needs further investigation (Murphy et al., 2013). Nevertheless, these results indicated that CD8α DC crosspriming of CD8 T cells during ECM required CCR7 that induces the expansion of effector CD11c+ CD8 T cells, which migrate into the brain via the OLF bulb, finally causing ECM. However, activated CD11c+ CD8 T cells migrate to brain via multiple molecules including several chemokines/chemokine receptors such as IP-10 and CXCR3 at the effector phase. It is evident in our study that CCL21 is involved in the priming of CD11c+ CD8 T cells; however, presence of CCL21 at OLF implied its association for the chemotactic support for T cell migration. The CXCR3 was recognized as an alternative receptor for CCL21, especially in astrocytes and microglia (van Weering et al., 2010), and CCL21was shown to be rapidly increased in the brain after *Toxoplasma* infection and supported T cell migration (Wilson et al., 2009). Therefore, it is plausible that CCL21 might be involved in the migration of CXCR3+ CD8 T cells into OLF. Our in vitro transwell migration assay supports this idea; however, limited effect of anti-CCL21 Ab treatment at the onset of OLF dysfunction (on day 4) might suggest compensation of other mechanisms causing pathology during effector phase of ECM in vivo. Nevertheless, here we show a "proof-of-concept" therapeutic approach that blocking CCL21 and/or combination blockage of CCR7-CCL21-CXCR3 axis could be exploited as a strategy for intervention during ECM.

In summary, this study demonstrates that the OLF bulb is a "weak spot" due to its complex architecture and could be a target for *Plasmodium* parasites which cause ECM. Murine studies have also concluded that immune cells such as pathogenic CD11c+ CD8 T cells enter brain via microbleedings at OLF. The CCL21 in the OLF GL during early infection might be one of the underlying mechanisms for the accumulation of pathogenic CD11c+ CD8 T cells, and CCL21 expression might be a risk factor for the development of ECM (Figure 7). These results provide evidence that OLF functional impairment is a valuable marker for ECM development and early diagnosis. Currently, whether these findings in mice are applicable to humans is unclear. Of note, the symptoms of OLF involvement in humans may differ from mice such as "olfactory hallucinations" (Barresi et al., 2012; Perry et al., 2009). Clearly, tests of olfaction loss and techniques such as improved human OLF MRI imaging (Wang et al., 2011) will be needed in future. Furthermore, OLF bulb as a location may be a useful therapeutic target for CM, as well as for various neuroimmune diseases in humans.

EXPERIMENTAL PROCEDURES

Parasites and Mice

Two different *Pb*A lines (with and without GFP) were used (Coban et al., 2007; Ishino et al., 2006; Zhao et al., 2012). The C57BL/6 (CLEA, Osaka, Japan), *Ccr7*$^{-/-}$ (kindly provided by Prof. M. Miyasaka and M.H. Jang (Osaka University) (Förster et al., 1999), and *Batf3*$^{-/-}$ (Jackson Labs) mice were used according to the guidelines of NIBIO and Osaka University.

Wild-type mice were i.v. injected daily with anti-CCL21 antibody or isotype control (50 μg per mouse, Peprotech) for 3 days from the beginning of infection. Alternatively, anti-CXCR3 antibody (LEAF-purified anti-mouse CD183 [CXCR3], 100 μg per mouse, Biolegend) was injected twice on days 4 and 5 after infection.

Buried Food Test

The BFT was performed as previously described (Yang and Crawley, 2009). Briefly, mice were left without food for 18 hr and were placed in a new cage containing buried food under the bedding. The time when the mouse found the buried food was recorded. The test was stopped at 15 min, and its time was recorded as 900 s (latency score, >>>).

MRI Brain Imaging

An ultra-high-field 11.7 T MRI scanner (AVANCE-II 500 WB; Bruker BioSpin) was used. Initially, naive live mice and 4% paraformaldehyde (PFA)-fixed dead mice heads were compared, and no significant differences were observed (Figure S1A). Therefore, in continuing experiments, infected and deeply anesthetized mice were fixed in PFA and visualized by MRI. The T_2* weighted (FLASH sequence) and DWIs (spin echo sequence) were used to detect bleedings.

Thinned-Skull Surgery and Multiphoton Imaging

The OLF bulb was visualized in living mice by previously described surgically "thinned-skull" technique (Sawada et al., 2011; Wake et al., 2009). Briefly, the mouse head was immobilized and the skull over the OLF was thinned (~20–30 μm). A metal ring was attached to the skull over the region and kept moist during imaging with a microscope (FV1000MPE, Olympus). OLF vasculature was visualized by tetramethylrhodamine isothiocyanate-dextran (5 mg, Sigma) and T cells by brilliant violet 421 conjugated TCR-β (10 μg, Biolegend) or CD8α (5 μg, Biolegend). A Ti-sapphire laser (MaiTai Hp, Spectral Physics) was tuned to the excitation wavelength 800 nm for T cells and vessels, and a Chameleon laser (Coherent) was tuned to 950 nm for GFP–*Pb*A. Time-lapse imaging of deep OLF regions (507.934 μm[x], 507.934 μm[y], 5 μm[z] per 1.1095 s) was performed by continuous repeated acquisition of fluorescence image stacks comprising 30–80 z planes (acquisition of one-stack image requires ~40–90 s). The typical imaging depth was 80–150 μm (Chaigneau et al., 2003). Each mouse was imaged only once. Imaging data were processed and analyzed using Volocity software.

Temperature Monitoring

A mouse cage with an in-house thermal monitoring system was developed (T.A., unpublished data and patent pending). A cage was prepared like an incubator, with an environmental temperature controlled at 30°C with a 12 hr light-dark cycle and food and water ad libitum. The back skin temperature was continuously recorded (after removing hair) at 1 min intervals by FLIR b60 thermal camera, and the data were analyzed by QuickPlot software (FLIR Systems, Inc.).

Assessment of BBB Permeability and Histology

At the indicated time points, mice were injected i.v. with 200 μl 1% of Evans blue dye (Sigma) and 2 hr later brains were removed, washed with PBS, and images taken. In addition, brains were removed and prepared for IHC as reported earlier (Zhao et al., 2012).

Quantitative Real-Time Reverse Transcription-PCR Analysis

Brain samples were homogenized, total RNA was isolated, and q-PCR was performed as described previously (Zhao et al., 2012).

Flow Cytometric Analysis

Spleen and brain cells were purified as described before (Coban et al., 2007; Zhao et al., 2012). Cell surfaces were stained for CD11c, CD4, CD8α, CD3, TCRβ, CCR7, CD44, CD11c, and CD11b.

Transwell Migration Assay

Forty-eight-well transwell plates (5 μm pore size, Costar, Corning Inc.) were used for chemotaxis assay as previously described (Rappert et al., 2002).

Adoptive Transfer Experiments

Total splenocytes were prepared from *Rag2*$^{-/-}$ mice 5 days after infection with *Pb*ANKA, and splenic CD8α+ DC were enriched with a purity >95% (Figure S5B).

Statistical Analysis

Differences between two groups were analyzed by using Prism software. The log rank (Mantel-Cox) test was performed for survival curves. $p < 0.05$ was considered statistically significant.

SUPPLEMENTAL INFORMATION

Supplemental Information includes seven figures, Supplemental Experimental Procedures, and five movies and can be found with this article at http://dx.doi.org/10.1016/j.chom.2014.04.008.

AUTHOR CONTRIBUTIONS

H.Z. performed IHC staining; A.K. infections, food test, and animal monitoring; Y.F. cell isolation, FACS staining, and qPCR; M.O. intracellular staining and transmigration assay; and M.S. parasitemia counts. H.Z., T.A., and Y.H. performed MP microscopy with help from K.E. and J.N.; M.K. helped FASC analysis; Y.M. and Y.Y. performed MRI; T.I. and M.Y. provided parasite lines; S.K., K.K., T.H., H.H., T.K., S.A., and K.J.I. contributed reagents and scientific advice; C.C., K.J.I., T.A., and Y.Y. wrote the manuscript; C.C. directed overall research.

ACKNOWLEDGMENTS

We thank Drs. K. Suzuki, W. Ise, and H. Arase (IFReC) for various discussions and support. This study was supported by grants from the Ministry of Education, Culture, Sports, Science and Technology in Japan (KAKENHI—Kiban B 25293100) and the Mochida Memorial Foundation for Medical and Pharmaceutical Research.

Received: December 16, 2013
Revised: March 5, 2014
Accepted: April 11, 2014
Published: May 14, 2014

REFERENCES

Baptista, F.G., Pamplona, A., Pena, A.C., Mota, M.M., Pied, S., and Vigário, A.M. (2010). Accumulation of Plasmodium berghei-infected red blood cells in the brain is crucial for the development of cerebral malaria in mice. Infect. Immun. *78*, 4033–4039.

Barresi, M., Ciurleo, R., Giacoppo, S., Foti Cuzzola, V., Celi, D., Bramanti, P., and Marino, S. (2012). Evaluation of olfactory dysfunction in neurodegenerative diseases. J. Neurol. Sci. *323*, 16–24.

Belnoue, E., Costa, F.T., Vigário, A.M., Voza, T., Gonnet, F., Landau, I., Van Rooijen, N., Mack, M., Kuziel, W.A., and Rénia, L. (2003a). Chemokine receptor CCR2 is not essential for the development of experimental cerebral malaria. Infect. Immun. *71*, 3648–3651.

Belnoue, E., Kayibanda, M., Deschemin, J.C., Viguier, M., Mack, M., Kuziel, W.A., and Rénia, L. (2003b). CCR5 deficiency decreases susceptibility to experimental cerebral malaria. Blood *101*, 4253–4259.

Bovetti, S., Hsieh, Y.C., Bovolin, P., Perroteau, I., Kazunori, T., and Puche, A.C. (2007). Blood vessels form a scaffold for neuroblast migration in the adult olfactory bulb. J. Neurosci. *27*, 5976–5980.

Cabrales, P., Zanini, G.M., Meays, D., Frangos, J.A., and Carvalho, L.J. (2010). Murine cerebral malaria is associated with a vasospasm-like microcirculatory dysfunction, and survival upon rescue treatment is markedly increased by nimodipine. Am. J. Pathol. *176*, 1306–1315.

Campanella, G.S., Tager, A.M., El Khoury, J.K., Thomas, S.Y., Abrazinski, T.A., Manice, L.A., Colvin, R.A., and Luster, A.D. (2008). Chemokine receptor CXCR3 and its ligands CXCL9 and CXCL10 are required for the development of murine cerebral malaria. Proc. Natl. Acad. Sci. USA *105*, 4814–4819.

Chaigneau, E., Oheim, M., Audinat, E., and Charpak, S. (2003). Two-photon imaging of capillary blood flow in olfactory bulb glomeruli. Proc. Natl. Acad. Sci. USA *100*, 13081–13086.

Chen, Y., Mancuso, J., Zhao, Z., Li, X., Cheng, J., Roman, G., and Wong, S.T. (2013). Vasodilation by in vivo activation of astrocyte endfeet via two-photon calcium uncaging as a strategy to prevent brain ischemia. J. Biomed. Opt. *18*, 126012.

Coban, C., Ishii, K.J., Uematsu, S., Arisue, N., Sato, S., Yamamoto, M., Kawai, T., Takeuchi, O., Hisaeda, H., Horii, T., and Akira, S. (2007). Pathological role of Toll-like receptor signaling in cerebral malaria. Int. Immunol. *19*, 67–79.

Danielyan, L., Schäfer, R., von Ameln-Mayerhofer, A., Buadze, M., Geisler, J., Klopfer, T., Burkhardt, U., Proksch, B., Verleysdonk, S., Ayturan, M., et al. (2009). Intranasal delivery of cells to the brain. Eur. J. Cell Biol. *88*, 315–324.

de Haas, A.H., van Weering, H.R., de Jong, E.K., Boddeke, H.W., and Biber, K.P. (2007). Neuronal chemokines: versatile messengers in central nervous system cell interaction. Mol. Neurobiol. *36*, 137–151.

De Saint Jan, D., and Westbrook, G.L. (2005). Detecting activity in olfactory bulb glomeruli with astrocyte recording. J. Neurosci. *25*, 2917–2924.

Förster, R., Schubel, A., Breitfeld, D., Kremmer, E., Renner-Müller, I., Wolf, E., and Lipp, M. (1999). CCR7 coordinates the primary immune response by establishing functional microenvironments in secondary lymphoid organs. Cell *99*, 23–33.

Hansen, D.S., Bernard, N.J., Nie, C.Q., and Schofield, L. (2007). NK cells stimulate recruitment of CXCR3+ T cells to the brain during Plasmodium berghei-mediated cerebral malaria. J. Immunol. *178*, 5779–5788.

Haque, A., Best, S.E., Unosson, K., Amante, F.H., de Labastida, F., Anstey, N.M., Karupiah, G., Smyth, M.J., Heath, W.R., and Engwerda, C.R. (2011). Granzyme B expression by CD8+ T cells is required for the development of experimental cerebral malaria. J. Immunol. *186*, 6148–6156.

Howland, S.W., Poh, C.M., Gun, S.Y., Claser, C., Malleret, B., Shastri, N., Ginhoux, F., Grotenbreg, G.M., and Renia, L. (2013). Brain microvessel cross-presentation is a hallmark of experimental cerebral malaria. EMBO Mol. Med. *5*, 916–931.

Idro, R., Marsh, K., John, C.C., and Newton, C.R. (2010). Cerebral malaria: mechanisms of brain injury and strategies for improved neurocognitive outcome. Pediatr. Res. *68*, 267–274.

Ishino, T., Orito, Y., Chinzei, Y., and Yuda, M. (2006). A calcium-dependent protein kinase regulates Plasmodium ookinete access to the midgut epithelial cell. Mol. Microbiol. *59*, 1175–1184.

Junt, T., Scandella, E., Förster, R., Krebs, P., Krautwald, S., Lipp, M., Hengartner, H., and Ludewig, B. (2004). Impact of CCR7 on priming and distribution of antiviral effector and memory CTL. J. Immunol. *173*, 6684–6693.

Kiyatkin, E.A., and Sharma, H.S. (2009). Permeability of the blood-brain barrier depends on brain temperature. Neuroscience *161*, 926–939.

Lalor, S.J., and Segal, B.M. (2010). Lymphoid chemokines in the CNS. J. Neuroimmunol. *224*, 56–61.

Lamb, T.J., Brown, D.E., Potocnik, A.J., and Langhorne, J. (2006). Insights into the immunopathogenesis of malaria using mouse models. Expert Rev. Mol. Med. *8*, 1–22.

Langhorne, J., Buffet, P., Galinski, M., Good, M., Harty, J., Leroy, D., Mota, M.M., Pasini, E., Renia, L., Riley, E., et al. (2011). The relevance of non-human primate and rodent malaria models for humans. Malar. J. *10*, 23.

Lundie, R.J., de Koning-Ward, T.F., Davey, G.M., Nie, C.Q., Hansen, D.S., Lau, L.S., Mintern, J.D., Belz, G.T., Schofield, L., Carbone, F.R., et al. (2008). Blood-stage Plasmodium infection induces CD8+ T lymphocytes to parasite-expressed antigens, largely regulated by CD8alpha+ dendritic cells. Proc. Natl. Acad. Sci. USA *105*, 14509–14514.

Machado, R.R., Soares, D.M., Proudfoot, A.E., and Souza, G.E. (2007). CCR1 and CCR5 chemokine receptors are involved in fever induced by LPS (E. coli) and RANTES in rats. Brain Res. *1161*, 21–31.

McLellan, A.D., Kapp, M., Eggert, A., Linden, C., Bommhardt, U., Bröcker, E.B., Kämmerer, U., and Kämpgen, E. (2002). Anatomic location and T-cell stimulatory functions of mouse dendritic cell subsets defined by CD4 and CD8 expression. Blood *99*, 2084–2093.

McQuillan, J.A., Mitchell, A.J., Ho, Y.F., Combes, V., Ball, H.J., Golenser, J., Grau, G.E., and Hunt, N.H. (2011). Coincident parasite and CD8 T cell sequestration is required for development of experimental cerebral malaria. Int. J. Parasitol. *41*, 155–163.

Medana, I.M., Chan-Ling, T., and Hunt, N.H. (1996). Redistribution and degeneration of retinal astrocytes in experimental murine cerebral malaria: relationship to disruption of the blood-retinal barrier. Glia *16*, 51–64.

Mesholam, R.I., Moberg, P.J., Mahr, R.N., and Doty, R.L. (1998). Olfaction in neurodegenerative disease: a meta-analysis of olfactory functioning in Alzheimer's and Parkinson's diseases. Arch. Neurol. *55*, 84–90.

Miragall, F., Krause, D., de Vries, U., and Dermietzel, R. (1994). Expression of the tight junction protein ZO-1 in the olfactory system: presence of ZO-1 on olfactory sensory neurons and glial cells. J. Comp. Neurol. *341*, 433–448.

Miu, J., Mitchell, A.J., Müller, M., Carter, S.L., Manders, P.M., McQuillan, J.A., Saunders, B.M., Ball, H.J., Lu, B., Campbell, I.L., and Hunt, N.H. (2008). Chemokine gene expression during fatal murine cerebral malaria and protection due to CXCR3 deficiency. J. Immunol. *180*, 1217–1230.

Miyakoda, M., Kimura, D., Yuda, M., Chinzei, Y., Shibata, Y., Honma, K., and Yui, K. (2008). Malaria-specific and nonspecific activation of CD8+ T cells during blood stage of Plasmodium berghei infection. J. Immunol. *181*, 1420–1428.

Mori, Y., Umeda, M., Fukunaga, M., Ogasawara, K., and Yoshioka, Y. (2011). MR contrast in mouse lymph nodes with subcutaneous administration of iron oxide particles: size dependency. Magn. Reson. Med. Sci. *10*, 219–227.

Murphy, T.L., Tussiwand, R., and Murphy, K.M. (2013). Specificity through cooperation: BATF-IRF interactions control immune-regulatory networks. Nat. Rev. Immunol. *13*, 499–509.

Nacer, A., Movila, A., Baer, K., Mikolajczak, S.A., Kappe, S.H., and Frevert, U. (2012). Neuroimmunological blood brain barrier opening in experimental cerebral malaria. PLoS Pathog. *8*, e1002982.

Netea, M.G., Kullberg, B.J., and Van der Meer, J.W. (2000). Circulating cytokines as mediators of fever. Clin. Infect. Dis. *31* (*Suppl 5*), S178–S184.

Noor, S., and Wilson, E.H. (2012). Role of C-C chemokine receptor type 7 and its ligands during neuroinflammation. J. Neuroinflammation *9*, 77.

Noor, S., Habashy, A.S., Nance, J.P., Clark, R.T., Nemati, K., Carson, M.J., and Wilson, E.H. (2010). CCR7-dependent immunity during acute Toxoplasma gondii infection. Infect. Immun. *78*, 2257–2263.

Perry, T.L., Pandey, P., Grant, J.M., and Kain, K.C. (2009). Severe atovaquone-resistant Plasmodium falciparum malaria in a Canadian traveller returned from the Indian subcontinent. Open Med. *3*, e10–e16.

Petzold, G.C., Albeanu, D.F., Sato, T.F., and Murthy, V.N. (2008). Coupling of neural activity to blood flow in olfactory glomeruli is mediated by astrocytic pathways. Neuron *58*, 897–910.

Piva, L., Tetlak, P., Claser, C., Karjalainen, K., Renia, L., and Ruedl, C. (2012). Cutting edge: Clec9A+ dendritic cells mediate the development of experimental cerebral malaria. J. Immunol. *189*, 1128–1132.

Rappert, A., Biber, K., Nolte, C., Lipp, M., Schubel, A., Lu, B., Gerard, N.P., Gerard, C., Boddeke, H.W., and Kettenmann, H. (2002). Secondary lymphoid tissue chemokine (CCL21) activates CXCR3 to trigger a Cl- current and chemotaxis in murine microglia. J. Immunol. *168*, 3221–3226.

Sawada, M., Kaneko, N., Inada, H., Wake, H., Kato, Y., Yanagawa, Y., Kobayashi, K., Nemoto, T., Nabekura, J., and Sawamoto, K. (2011). Sensory input regulates spatial and subtype-specific patterns of neuronal turnover in the adult olfactory bulb. J. Neurosci. *31*, 11587–11596.

Strous, R.D., and Shoenfeld, Y. (2006). To smell the immune system: olfaction, autoimmunity and brain involvement. Autoimmun. Rev. *6*, 54–60.

Tamura, T., Kimura, K., Yuda, M., and Yui, K. (2011). Prevention of experimental cerebral malaria by Flt3 ligand during infection with Plasmodium berghei ANKA. Infect. Immun. *79*, 3947–3956.

Taylor, T.E., Fu, W.J., Carr, R.A., Whitten, R.O., Mueller, J.S., Fosiko, N.G., Lewallen, S., Liomba, N.G., and Molyneux, M.E. (2004). Differentiating the pathologies of cerebral malaria by postmortem parasite counts. Nat. Med. *10*, 143–145.

Van den Steen, P.E., Deroost, K., Van Aelst, I., Geurts, N., Martens, E., Struyf, S., Nie, C.Q., Hansen, D.S., Matthys, P., Van Damme, J., and Opdenakker, G. (2008). CXCR3 determines strain susceptibility to murine cerebral malaria by mediating T lymphocyte migration toward IFN-gamma-induced chemokines. Eur. J. Immunol. *38*, 1082–1095.

van Weering, H.R., de Jong, A.P., de Haas, A.H., Biber, K.P., and Boddeke, H.W. (2010). CCL21-induced calcium transients and proliferation in primary mouse astrocytes: CXCR3-dependent and independent responses. Brain Behav. Immun. *24*, 768–775.

Wake, H., Moorhouse, A.J., Jinno, S., Kohsaka, S., and Nabekura, J. (2009). Resting microglia directly monitor the functional state of synapses in vivo and determine the fate of ischemic terminals. J. Neurosci. *29*, 3974–3980.

Wang, J., You, H., Liu, J.F., Ni, D.F., Zhang, Z.X., and Guan, J. (2011). Association of olfactory bulb volume and olfactory sulcus depth with olfactory function in patients with Parkinson disease. AJNR Am. J. Neuroradiol. *32*, 677–681.

Whitman, M.C., Fan, W., Rela, L., Rodriguez-Gil, D.J., and Greer, C.A. (2009). Blood vessels form a migratory scaffold in the rostral migratory stream. J. Comp. Neurol. *516*, 94–104.

Wilson, E.H., Harris, T.H., Mrass, P., John, B., Tait, E.D., Wu, G.F., Pepper, M., Wherry, E.J., Dzierzinski, F., Roos, D., et al. (2009). Behavior of parasite-specific effector CD8+ T cells in the brain and visualization of a kinesis-associated system of reticular fibers. Immunity *30*, 300–311.

Yang, M., and Crawley, J.N. (2009). Simple behavioral assessment of mouse olfaction. Curr. Protoc. Neurosci. *Chapter 8*, Unit 8 24.

Zhao, H., Konishi, A., Fujita, Y., Yagi, M., Ohata, K., Aoshi, T., Itagaki, S., Sato, S., Narita, H., Abdelgelil, N.H., et al. (2012). Lipocalin 2 bolsters innate and adaptive immune responses to blood-stage malaria infection by reinforcing host iron metabolism. Cell Host Microbe *12*, 705–716.

Vaccine 32 (2014) 3004–3009

Contents lists available at ScienceDirect

Vaccine

journal homepage: www.elsevier.com/locate/vaccine

Hemozoin is a potent adjuvant for hemagglutinin split vaccine without pyrogenicity in ferrets

Motoyasu Onishi[a,b,c], Mitsutaka Kitano[a], Keiichi Taniguchi[a], Tomoyuki Homma[a], Masanori Kobayashi[a], Akihiko Sato[a], Cevayir Coban[d], Ken J. Ishii[b,c,*]

[a] Infectious Diseases, Medicinal Research Laboratories, Shionogi & Co., Ltd., Osaka, Japan
[b] Laboratory of Adjuvant Innovation, National Institute of Biomedical Innovation (NIBIO), Osaka, Japan
[c] Laboratory of Vaccine Science, Immunology Frontier Research Center (IFREC), World Premier Institute (WPI), Osaka University, Osaka, Japan
[d] Laboratory of Malaria Immunology, Immunology Frontier Research Center (IFREC), World Premier Institute (WPI), Osaka University, Osaka, Japan

ARTICLE INFO

Article history:
Received 21 November 2013
Received in revised form 14 February 2014
Accepted 25 March 2014
Available online 8 April 2014

Keywords:
Vaccine
Adjuvant
Influenza
Fluad
Ferret
Seasonal trivalent HA split vaccine

ABSTRACT

Background: Synthetic hemozoin (sHZ, also known as β-hematin) from monomeric heme is a particle adjuvant which activates antigen-presenting cells (APCs), such as dendritic cells and macrophages, and enhances humoral immune responses to several antigens, including ovalbumin, human serum albumin, and serine repeat antigen 36 of *Plasmodium falciparum*. In the present study, we evaluated the adjuvanticity and pyrogenicity of sHZ as an adjuvant for seasonal trivalent hemagglutinin split vaccine (SV) for humans using the experimental ferret model.
Method: Ferrets were twice immunized with trivalent SV, SV with sHZ (SV/sHZ) or Fluad, composed of trivalent SV with MF59. Serum hemagglutination inhibition (HI) titers against three viral hemagglutinin (HA) antigens were measured at every week after the immunization. The pyrogenicity of SV/sHZ was examined by monitoring the body temperature of the immunized ferrets. To evaluate the protective efficacy of SV/sHZ, the immunized ferrets were challenged with influenza virus B infection, followed by measurement of viral titers in the nasal cavity and body temperature.
Results: sHZ enhanced HI titers against three viral HA antigens in a dose-dependent manner, to an extent comparable to that of Fluad. The highest dose of sHZ (800 μg) immunized with SV conferred sterile protection against infection with heterologous Influenza B virus, without causing any pyrogenic reaction such as high fever.
Conclusion: In the present study, sHZ enhanced the protective efficacy of SV against influenza infection without inducing pyrogenic reaction, suggesting sHZ to be a promising adjuvant candidate for human SV.

1. Introduction

Hemozoin (HZ) is a detoxification product of heme molecules persisting in the food vacuoles of *Plasmodium* parasite [1,2]. Purified HZ activates innate immune responses via Toll-like receptor (TLR)9 in antigen-presenting cells (APCs), including myeloid and plasmacytoid dendritic cells [3], and enhances humoral responses depending TLR9 but not NACHT, LRR and PYD domains containing the protein 3 (NALP3) inflammasome signaling pathway [4]. Synthetic hemozoin (sHZ, also known as β-hematin) from monomeric heme also activates APCs, and enhances the humoral responses of several antigens, including ovalbumin, human serum albumin, and serine repeat antigen 36 of *Plasmodium falciparum* in mice or cynomolgus monkeys (*Macaca fascicularis*) [4,5]. Moreover, sHZ acts as a potent immune modulator, which suppresses IgE production against house dust allergens, suggesting that sHZ itself might be usable for an allergy vaccine for dogs [4]. Differently from the purified HZ, sHZ enhance the adaptive immune response through MyD88, not related to TLR9 or NALP3 inflammasome pathway [4]. Thus, the efficacy, safety, and immunological mechanisms of sHZ has been demonstrated, further studies are needed to explore its application as an adjuvant for vaccines.

In general, the efficacy of influenza hemagglutinin split vaccine (SV) correlates with the level of neutralizing antibody to

Abbreviations: sHZ, synthetic hemozoin; HA, hemagglutinin; HI, hemagglutination inhibition; SV, hemagglutinin split vaccine; SV/sHZ, hemagglutinin split vaccine adjuvanted with synthetic hemozoin; $TCID_{50}$, 50% tissue culture infective dose.

* Corresponding author at: NIBIO, 7-6-8 Asagi, Saito, Ibaraki, Osaka 5670085, Japan. Tel.: +81 72 641 8043; fax: +81 72 641 8079.
E-mail addresses: kenishii@biken.osaka-u.ac.jp, kenishii@nibio.go.jp (K.J. Ishii).

http://dx.doi.org/10.1016/j.vaccine.2014.03.072

hemagglutinin (HA) [6]. The neutralizing antibody contributes to both prevention of influenza infection and suppression of influenza exacerbation. Some reports have estimated the efficacy of influenza vaccine in young adults to be 70–90%, and that in the elderly to be considerably lower, in the range of 17–53% [7]. Hence, SV is required to improve the efficacy for the elderly. One possible solution of the issue is via the use of adjuvant [8], although some adjuvants have been reported to cause pyrogenic reaction associated with the induction of proinflammatory cytokine responses in clinical studies [9,10]. Therefore, it is important to evaluate the pyrogenicity of adjuvant in clinical or non-clinical studies to enable wider use of adjuvants.

In the present study, we evaluated the efficacy and pyrogenicity of sHZ as an adjuvant for seasonal trivalent SV in the ferret model.

2. Materials and methods

2.1. Antigens and adjuvants

Seasonal influenza SV "BIKEN", containing influenza virus HA surface antigens from three virus strains, A/California/7/2009 (H1N1), A/Victoria/210/2009 (H3N2), and B/Brisbane/60/2008, was obtained from The Research Foundation for Microbial Diseases of Osaka University (Osaka, Japan) [11]. Endotoxin-free sHZ chemically synthesized using an acidic method was obtained from Invivogen (San Diego, CA) [12]. The particle size of sHZ was determined by SEM and found to be approximately 1–2 μm. Fluad, composed of influenza virus HA surface antigens from the three strains described above and MF59, was obtained from Novartis Vaccines and Diagnostics, Inc. (Emeryville, CA) [13].

2.2. Virus and cells

Influenza virus B/Osaka/32/2009 was kindly provided by Osaka Prefectural Institute of Public Health. Madin–Darby canine kidney (MDCK) cells were obtained from the American Type Culture Collection (Manassas, VA) and were grown in minimum essential medium (MEM; Invitrogen, Carlsbad, CA) supplemented with 10% fetal bovine serum (Invitrogen) and 100 μg/ml kanamycin sulfate (Invitrogen) in a humidified atmosphere of 5% CO_2 at 37 °C.

2.3. Ferrets

Approximately 7- to 8-month-old female ferrets were purchased from Marshall Bioresources Japan Inc. (Ibaragi, Japan) and Japan SLC Inc. (Shizuoka, Japan). The experiments were performed under applicable laws and guidelines and after approval from the Shionogi Animal Care and Use Committee. Under anesthesia, at least 1 week before virus inoculation, a data logger (DS1921H-F5; Maxim Integrated Products, Inc., Sunnyvale, CA) was subcutaneously implanted into each ferret to monitor body temperature as previously reported [14]. The absence of influenza A/California/7/2009 (H1N1), A/Victoria/210/2009 (H3N2), and B/Brisbane/60/2008 virus-specific antibody in serum from each ferret was confirmed by hemagglutination inhibition (HI) test before the first immunization.

2.4. HI assay

HI assay was performed according to the protocol previously reported [14]. Serum was treated with receptor-destroying enzyme (RDEII; Denka Seiken, Tokyo, Japan). Serially diluted sera were mixed with 4 HA units of virus antigen for 1 h at room temperature. The mixture was then incubated with 0.5% chicken red blood cells for 30 min at room temperature. The HI titers were expressed as reciprocals of the highest dilution of serum samples that completely inhibited hemagglutination.

2.5. Immunization and sample collection

Ferrets were subcutaneously immunized with 22.5 μg of SV, 22.5 μg of SV adjuvanted with 50–800 μg of sHZ (SV/sHZ (50–800 μg)) or premix solution Fluad, which is composed of 22.5 μg of SV and MF59. Second immunizations were conducted 28 days after the first immunization. Serum was collected by vena cava puncture on the day of the first immunization and 7, 14, 21, 28, and 35 days after the first immunization, and HI titers against three HA antigens, A/California/7/2009 (H1N1), A/Victoria/210/2009 (H3N2), and B/Brisbane/60/2008, were determined.

2.6. Evaluation of pyrogenicity of vaccine with adjuvant in ferrets

Ferrets were subcutaneously immunized with saline or 22.5 μg of SV adjuvanted with 800 μg of sHZ. Body temperatures were monitored every 15 min with the data logger implanted in the ferrets.

2.7. Evaluation of protective effect of vaccine against influenza virus infection

Under anesthesia, ferrets were inoculated intranasally with B/Osaka/32/2009 (1.0×10^4 $TCID_{50}$) in 400 μl of phosphate-buffered saline (PBS). To monitor virus replication in nasal cavities, nasal washes were collected from infected ferrets on days 1 to 6 after infection. The collected samples were stored at below −80 °C until use. For virus titration, serial dilutions of nasal washes were inoculated onto confluent MDCK cells in 96-well plates. After 1 h incubation, the suspension was removed, and the cells were cultured in MEM including 0.5% bovine serum albumin (BSA; Sigma-Aldrich) and 3 μg/ml trypsin. The plates were incubated at 37 °C in 5% CO_2 for 3 days. The presence of cytopathic effects (CPEs) was determined under a microscope, and viral titers were calculated as $\log_{10}$ of $TCID_{50}$/ml. When no CPE was observed using undiluted viral solution, it was defined as an undetectable level, which was considered to be lower than 1.4 $\log_{10}$ of $TCID_{50}$/ml.

2.8. Activation of the inflammasome in peritoneal resident macrophages

Activation of the inflammasome in peritoneal resident macrophages was examined according to the protocol previously reported [15]. Briefly, peritoneal resident macrophages were collected from C57BL/6 mice (Charles River Laboratories Japan, Inc., Kanagawa, Japan) and were prepared with complete RPMI1640 medium (Invitrogen). Macrophages were primed with 50 ng/ml LPS (Sigma-Aldrich) for 18 h and then stimulated with sHZ or Alum (Invivogen) for 8 h. The concentration of IL-1β in supernatant was measured by ELISA (R&D systems, Minneapolis, MN).

2.9. Statistical analysis

Viral titers and body temperature of each animal were calculated as the area under the curve (AUC) by the trapezoidal method. Statistical significance between groups was determined by Dunnett's multiple comparison test using the statistical analysis software SAS (version 9.2) for Windows (SAS Institute, Cary, NC).

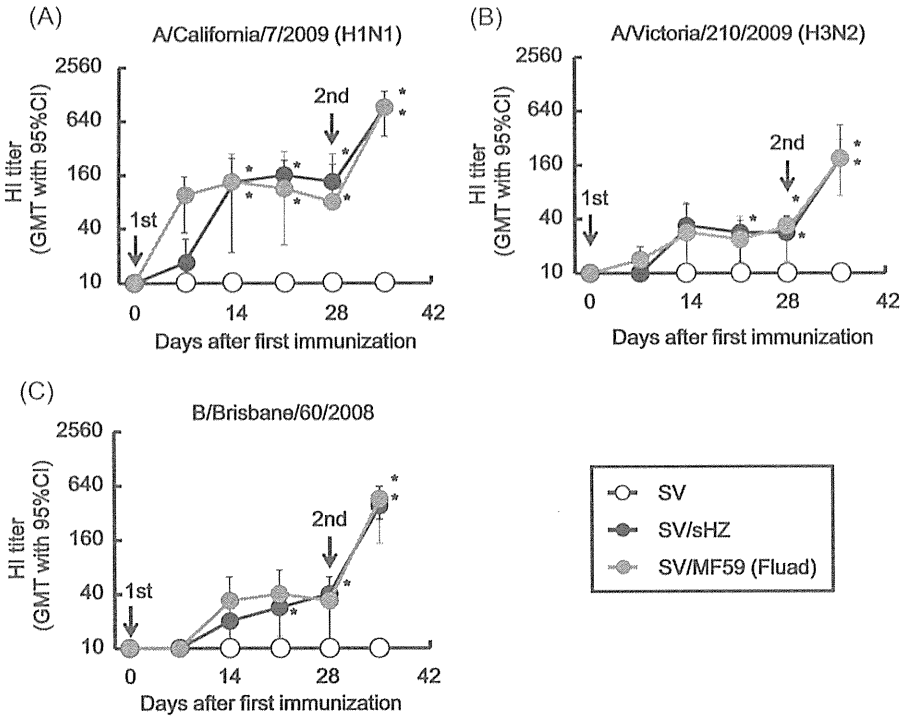

Fig. 1. Evaluation of the immunogenicity of SV, SV/sHZ, and Fluad. Ferrets were twice immunized with SV, SV/sHZ (800 μg) or Fluad. Serum were collected on day 0, 7, 14, 21, 28, and 35 after the first immunization, and HI titers against three HA antigens of A/California/7/2009(H1N1) (A), A/Victoria/210/2009 (H3N2) (B), and B/Brisbane/60/2008 (C) were measured. * $p < 0.05$ by Dunnett's multiple comparison test vs. SV group ($n = 4$ per group). Data represent the GMT ± 95% confidence interval.

3. Results

3.1. sHZ enhanced immunogenicity of HA split vaccine in a dose-dependent manner

To examine the adjuvant effect of sHZ on HA split vaccine, ferrets ($n = 4$ per group) were twice immunized with SV with or without sHZ (800 μg) or Fluad, and then their serum HI titers were measured every week. Fluad is composed of SV adjuvanted with MF59, a licensed squalene-based emulsion, widely used in clinical settings [16]. On day 28 after the first immunization, HI titers of SV/sHZ group against H1, H3, and B virus antigens were significantly up-regulated, of which the GMT was 135, 28, and 40, respectively, comparable to those elicited by MF59 ($p < 0.05$, Fig. 1A–C). After the second immunization, HI titers of the SV/sHZ group against all three antigens were significantly higher than those of the SV group on day 35 ($p < 0.05$) (Fig. 1A–C). The GMTs of the HI titers against H1, H3, and B antigens in the SV/sHZ group were 905, 190, and 381, respectively. The boosting effect of sHZ was also comparable to that of MF59. By contrast, HI titers against three HA antigens of the SV group were not enhanced at every analysis point (Fig. 1A–C). These results demonstrated that sHZ has a potent adjuvanticity to enhance the immunogenicity of SV, and its activity was comparable to that of MF59 in ferrets.

Next, the dose-dependent adjuvanticity of sHZ to enhance the immunogenicity of SV was examined. Ferrets were twice immunized with SV/sHZ (50–800 μg), and HI titers were measured at every week. The adjuvanticity to enhance HI titers against HA antigens of H1 and B was observed with at least 200 μg of sHZ after the first immunization, but no boosting effect of 200 μg of sHZ was observed after the second immunization (Fig. 2). Overall, each HI titer against all three HA antigens of SV/sHZ (800 μg) was 3–20 fold higher than that of SV/sHZ (200 μg) on day 7 after the second immunization. Thus, 800 μg of sHZ showed higher adjuvanticity than 200 μg of sHZ. This result implied that sHZ enhanced the immunogenicity of SV in a dose-dependent manner in ferrets.

3.2. HA split vaccine adjuvanted with sHZ did not cause pyrogenic reaction after immunization

It is reported that the ferret model can evaluate not only the efficacy of vaccine but also the pyrogenicity of immunostimulatory agents like TLR ligands (e.g. TLR7/8 agonist R848) and virion components, and non-pyrogenicity of SV [17,18] To evaluate the pyrogenicity of sHZ after the first immunization, ferrets were immunized with saline or SV/sHZ (800 μg), and the body temperatures of ferrets were monitored continuously. The results showed that sHZ did not enhance the body temperature after immunization, and no difference was observed in body temperature between the SV/sHZ and the saline groups, suggesting that sHZ does not have the potential to induce a pyrogenic reaction in ferrets (Fig. 3).

3.3. sHZ enhanced the protective efficacy of HA split vaccine against influenza virus infection

Having observed such potent adjuvanticity without pyrogenicity of sHZ in ferrets, we next evaluated the contribution of sHZ-adjuvanted SV vaccine to its protective efficacy. On day 7 after the second immunization, the ferrets were intranasally infected with B/Osaka/32/2009, and viral titers in nasal cavities were measured daily after infection. On day 2 after infection, each viral titer of two groups SV/sHZ (200 μg) and SV/sHZ (800 μg) was significantly lower than that of the SV group ($p < 0.01$ and <0.001, respectively) (Fig. 4A). Each viral titer AUC of SV/sHZ (200 μg and 800 μg) groups was significantly lower than that of the SV group ($p < 0.01$) (Fig. 4C).

The body temperature changes of ferrets were monitored from 2 days before to 5 days after infection. Comparing the SV group with the SV/sHZ group showed that the elevations of body temperature

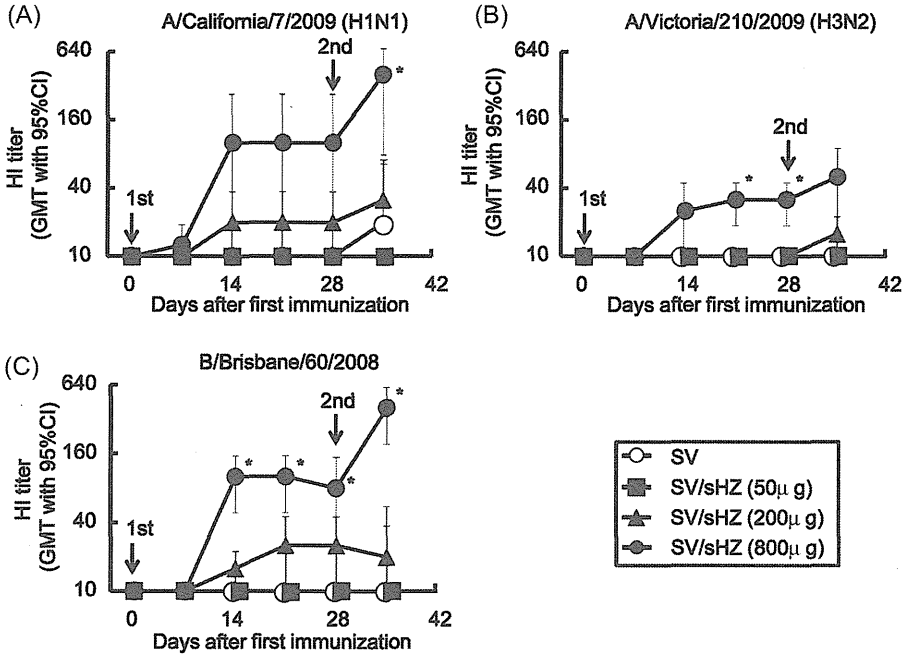

Fig. 2. Evaluation of the dose responses of sHZ to enhance HI antibody responses against three HA antigens. Ferrets were twice immunized with SV ($n = 6$) or SV/sHZ (50, 200 or 800 μg) ($n = 3$). Serum were collected on day 0, 7, 14, 21, 28, and 35 after the first immunization, and HI titers against three HA antigens of A/California/7/2009(H1N1) (A), A/Victoria/210/2009 (H3N2) (B), and B/Brisbane/60/2008 (C) were measured. * $p < 0.05$ by Dunnett's multiple comparison test vs. SV group. Data represent the GMT ± 95% confidence interval.

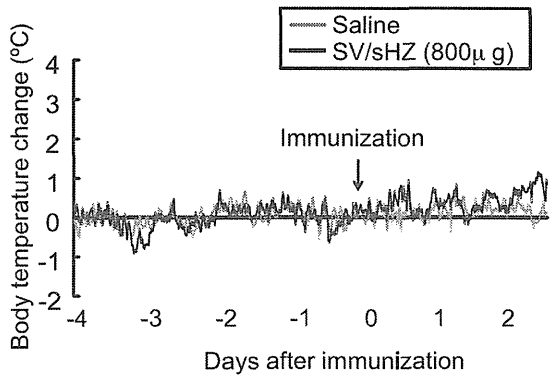

Fig. 3. Evaluation of pyrogenicity of SV/sHZ. Ferrets were immunized with saline or SV/sHZ (800 μg) ($n = 2$–3). Body temperatures of ferrets were recorded every 15 min by a data logger which had been implanted subcutaneously. The data were plotted from the average of body temperature changes every 15 min. Gray and black lines indicate the saline and the SV/sHZ groups, respectively. Baseline was set as the average of body temperature during the 2 days before immunization.

were suppressed in all SV/sHZ groups in a dose-dependent manner (Fig. 4B). Moreover, body temperature change AUCs of all SV/sHZ groups were lower than that of the SV vaccine group (Fig. 4D).

4. Discussion

Vaccination is the primary strategy to prevent influenza infection [19]. The efficacy of influenza vaccine in young and healthy adults is estimated to be 70–90%, but that in the elderly is lower at 17–53% [7]. Dose escalation of antigen has been examined to enhance the efficacy of vaccine for the elderly [20]. However, this is not a realistic approach without improvement of the manufacturing plants or manufacturing systems. As an alternative strategy, the use of adjuvant may help overcome these issues by enhancing the immunogenicity of influenza vaccine. In the present study, sHZ enhanced the immunogenicity of SV and consequently elevated its protective efficacy against virus infection in the ferret model, which has been shown to reflect influenza symptoms and protective immune responses to influenza infection in humans [21]. In particular, SV/sHZ (800 μg) strongly suppressed the viral titer below the detection limit and did not cause pyrogenic reaction after immunization. These results suggested sHZ to be a promising adjuvant candidate for human SV.

Pyrogenicity is one of the main issues in the development of novel adjuvants for vaccine even with good adjuvanticity. Therefore, minimizing toxicity remains one of the major challenges in adjuvant research [22]. Treanor et al. reported that VAX125, a recombinant HA influenza-flagellin fusion vaccine, showed high immunogenicity in clinical study [23], but in some cases, febrile symptoms were observed in the first 24 h following vaccination. It was suggested that the pyrogenic reaction was associated with systemic proinflammatory cytokine responses. sHZ induces the production of IL-1β by activating NALP3 inflammasome pathway in macrophages [24,25]. However, in the present study, sHZ did not cause pyrogenic reaction after the first immunization. To find insights into why sHZ did not show pyrogenicity, the activity of sHZ to induce the NALP3 inflammasome was examined, and the results revealed that a relatively high concentration (≥300 μg/ml) of sHZ was required to induce IL-1β production in macrophages (Supplemental Fig. 1). Dostert et al. also demonstrated that 150 μg/ml sHZ could induce inflammasome in bone marrow-derived macrophages [25]. These results suggested that the activation of NALP3-inflammasome caused by sHZ was very low and did not act as a trigger to cause a pyrogenic reaction in ferrets.

Rapid systemic distribution of adjuvant is also understood to enhance the risk of causing a pyrogenic reaction. Sauder et al. reported that R848, which is known as an imidazoquinoline compound and TLR7/8 agonist, caused a pyrogenic reaction correlated

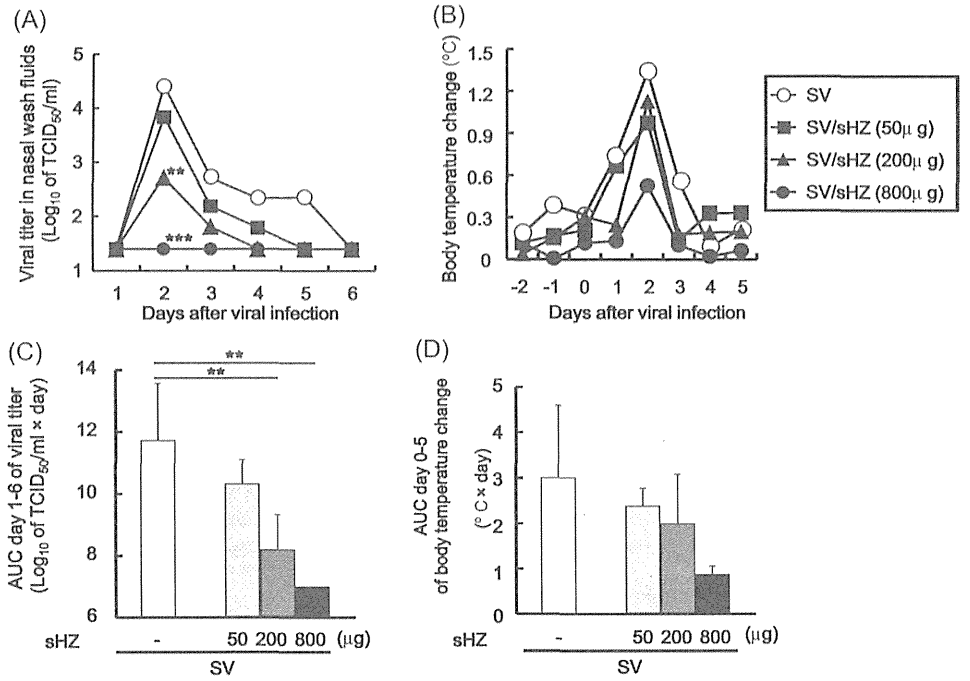

Fig. 4. Evaluation of the protective efficacy of SV/sHZ against virus infection. B/Osaka/32/2009 (1.0×10^4 $TCID_{50}$) was intranasally infected to ferrets immunized with SV ($n = 6$) or SV/sHZ (50, 200 or 800 μg) ($n = 3$). Nasal wash fluids were collected on days 1–6 after infection, and viral titers were measured (A). Data represent the means. Viral titer AUCs were calculated using the trapezoidal rule on the basis of means of the viral titers ($TCID_{50}$/ml) on days 1 to 6 (C). Data represent the mean ± standard deviation. Body temperatures of ferrets were recorded every 60 min by data logger which had been subcutaneously implanted. The baseline of the body temperature was set as the average of body temperature during the 2 days before infection. The data were plotted from the average of body temperature changes during 1 day (B). Data represent the mean. Body temperature change AUCs were calculated by use of the trapezoidal rule on the basis of the means of the body temperature change on days 0 to 5 (D). Data represent the mean ± standard deviation. ** $p < 0.01$, *** $p < 0.001$ by Dunnett's multiple comparison test vs. SV group.

with the induction of proinflammatory cytokine responses in healthy adults [10]. This strong response was caused by rapid systemic distribution of R848 after administration [10]. 3M-052 is a lipid-modified imidazoquinoline compound derived from R848, bearing a C18 lipid moiety, for sustained release and incorporation into a bilayer liposome [26]. 3M-052 incorporated into liposome composed of dioleoylphosphatidylcholine (3M-052/PC) was shown to avoid the induction of systemic proinflammatory cytokine responses [26]. In addition, the adjuvanticity of 3M-052/PC was higher than that of R848. Therefore, persistent immunostimulation at the injected site with adjuvant is thought to contribute to its potent adjuvanticity [26]. sHZ, synthesized by an acidic method, formed insoluble particles approximately 1–2 μm in size. On day 35 after the first immunization, a small amount of sHZ was observed at the immunized site (data not shown), suggesting that the distribution of sHZ was not rapid or was very limited in ferrets. Thus, slow systemic distribution of sHZ might contribute to prevent a pyrogenic reaction and maintain potent adjuvanticity after immunization. The size of particle adjuvant is considered to affect the particulate-induced immune responses such as the efficient activation of dendritic cells or adjuvant uptake of macrophages [27]. The smaller particles (20–200 nm) are usually uptaken by endocytosis via clathrin-coated vesicles, caveolae or their independent receptors, and preferentially ingested by dendritic cells. The larger size particles (0.5–5 μm) are uptaken by macropinocytosis, while particles greater than 0.5 μm are predominantly taken up by phagocytosis, and primarily ingested by macrophages [28]. The crystal size of sHZ can be adjusted by the modification of synthetic method, and smaller size sHZ (diameter range; 50 nm–1 μm, peak of the frequency distribution; 50–200 nm) exhibits higher adjuvanticity than larger size sHZ (>5 μm) in mice when immunized with ovalbumin antigen [4]. This size-dependent adjuvanticity of sHZ is considered as the result from the manner of uptake of APCs. In this study, we demonstrated the potent adjuvanticity of sHZ, which contains approximately 1–2 μm particles.

In the present study, we demonstrated that sHZ could enhance the protective efficacy of SV against influenza virus in ferrets without causing a pyrogenic reaction. The findings of this study indicate that sHZ is safe and has great potential for use as an adjuvant for human SV.

Funding sources

This study was financially supported by Shionogi & Co., Ltd. a contrated collaboration between NIBIO and Shionogi & Co., Ltd.

Author contributions

M.O., M. Kitano, K.T., T.H., M. Kobayashi, A.S., and K.J.I. designed research; M.O., M. Kitano, K.T., T.H., and M. Kobayashi performed research; M.O., M. Kitano, and K.T. analyzed data; M.O. drafted the article; T.H., C.C. and K.J.I. revised the article critically for important intellectual content.

Conflict of interest statement

CC and KJI hold a patent related to synthetic hemozoin. The other authors declare no conflict of interest.

Acknowledgments

We thank Tetsuo Kase from the Osaka Prefectural Institute of Public Health for providing B/Osaka/32/2009 and Makoto Kodama

from Shionogi & Co., Ltd. for help with the animal care and experiments.

Appendix A. Supplementary data

Supplementary material related to this article can be found, in the online version, at http://dx.doi.org/10.1016/j.vaccine.2014.03.072.

References

[1] Sullivan DJ. Theories on malarial pigment formation and quinoline action. Int J Parasitol 2002;32(13):1645–53.
[2] Arese P, Schwarzer E. Malarial pigment (haemozoin): a very active 'inert' substance. Ann Trop Med Parasitol 1997;91(5):501–16.
[3] Coban C, Ishii KJ, Kawai T, Hemmi H, Sato S, Uematsu S, et al. Toll-like receptor 9 mediates innate immune activation by the malaria pigment hemozoin. J Exp Med 2005;201(1):19–25.
[4] Coban C, Igari Y, Yagi M, Reimer T, Koyama S, Aoshi T, et al. Immunogenicity of whole-parasite vaccines against *Plasmodium falciparum* involves malarial hemozoin and host TLR9. Cell Host Microbe 2010;7(1):50–61.
[5] Tougan T, Aoshi T, Coban C, Katakai Y, Kai C, Yasutomi Y, et al. TLR9 adjuvants enhance immunogenicity and protective efficacy of the SE36/AHG malaria vaccine in nonhuman primate models. Hum Vaccines Immunother 2013;9(2):283–90.
[6] Cox RJ, Brokstad KA, Ogra P. Influenza virus: immunity and vaccination strategies. Comparison of the immune response to inactivated and live, attenuated influenza vaccines. Scand J Immunol 2004;59(1):1–15.
[7] Goodwin K, Viboud C, Simonsen L. Antibody response to influenza vaccination in the elderly: a quantitative review. Vaccine 2006;24(8):1159–69.
[8] Tetsutani K, Ishii KJ. Adjuvants in influenza vaccines. Vaccine 2012;30(52):7658–61.
[9] Batista-Duharte A, Lindblad EB, Oviedo-Orta E. Progress in understanding adjuvant immunotoxicity mechanisms. Toxicol Lett 2011;203(2):97–105.
[10] Sauder DN, Smith MH, Senta-McMillian T, Soria I, Meng TC. Randomized, single-blind, placebo-controlled study of topical application of the immune response modulator resiquimod in healthy adults. Antimicrob Agents Chemother 2003;47(12):3846–52.
[11] Tanimoto T, Nakatsu R, Fuke I, Ishikawa T, Ishibashi M, Yamanishi K, et al. Estimation of the neuraminidase content of influenza viruses and split-product vaccines by immunochromatography. Vaccine 2005;23(37):4598–609.
[12] Coban C, Yagi M, Ohata K, Igari Y, Tsukui T, Horii T, et al. The malarial metabolite hemozoin and its potential use as a vaccine adjuvant. Allergol Int 2010;59(2):115–24.
[13] Puig Barbera J, Gonzalez Vidal D. MF59-adjuvanted subunit influenza vaccine: an improved interpandemic influenza vaccine for vulnerable populations. Expert Rev Vaccines 2007;6(5):659–65.
[14] Kitano M, Itoh Y, Kodama M, Ishigaki H, Nakayama M, Ishida H, et al. Efficacy of single intravenous injection of peramivir against influenza B virus infection in ferrets and cynomolgus macaques. Antimicrob Agents Chemother 2011;55(11):4961–70.
[15] Kuroda E, Ishii KJ, Uematsu S, Ohata K, Coban C, Akira S, et al. Silica crystals and aluminum salts regulate the production of prostaglandin in macrophages via NALP3 inflammasome-independent mechanisms. Immunity 2011;34(4):514–26.
[16] Della Cioppa G, Nicolay U, Lindert K, Leroux-Roels G, Clement F, Castellino F, et al. Superior immunogenicity of seasonal influenza vaccines containing full dose of MF59 ((R)) adjuvant: results from a dose-finding clinical trial in older adults. Hum Vaccines Immunother 2012;8(2):216–27.
[17] Kitano M, Homma T, Taniguchi K, Oonishi M, Kobayashi M, Sato A, et al. Pyrogenicity evaluation of influenza vaccine with TLR agonists in ferret. In: Sixth Vaccine & ISV Annual Global Congress. 2012.
[18] Pickering JM, Smith H, Sweet C. Influenza virus pyrogenicity: central role of structural orientation of virion components and involvement of viral lipid and glycoproteins. J Gen Virol 1992;73(Pt 6):1345–54.
[19] Lambert LC, Fauci AS. Influenza vaccines for the future. N Engl J Med 2010;363(21):2036–44.
[20] Couch RB, Winokur P, Brady R, Belshe R, Chen WH, Cate TR, et al. Safety and immunogenicity of a high dosage trivalent influenza vaccine among elderly subjects. Vaccine 2007;25(44):7656–63.
[21] Matsuoka Y, Lamirande EW, Subbarao K. The ferret model for influenza. Curr Protoc Microbiol 2009;2 (Chapter 15:Unit 15G).
[22] Aguilar JC, Rodriguez EG. Vaccine adjuvants revisited. Vaccine 2007;25(19):3752–62.
[23] Treanor JJ, Taylor DN, Tussey L, Hay C, Nolan C, Fitzgerald T, et al. Safety and immunogenicity of a recombinant hemagglutinin influenza-flagellin fusion vaccine (VAX125) in healthy young adults. Vaccine 2010;28(52):8268–74.
[24] Shio MT, Eisenbarth SC, Savaria M, Vinet AF, Bellemare MJ, Harder KW, et al. Malarial hemozoin activates the NLRP3 inflammasome through Lyn and Syk kinases. PLoS Pathog 2009;5(8):e1000559.
[25] Dostert C, Guarda G, Romero JF, Menu P, Gross O, Tardivel A, et al. Malarial hemozoin is a Nalp3 inflammasome activating danger signal. PLoS One 2009;4(8):e6510.
[26] Smirnov D, Schmidt JJ, Capecchi JT, Wightman PD. Vaccine adjuvant activity of 3M-052: an imidazoquinoline designed for local activity without systemic cytokine induction. Vaccine 2011;29(33):5434–42.
[27] Kuroda E, Coban C, Ishii K. Particulate adjuvant and innate immunity: past achievements, present findings, and future prospects. Int Rev Immunol 2013;32(2):209–20.
[28] Xiang SD, Scholzen A, Minigo G, David C, Apostolopoulos V, Mottram PL, et al. Pathogen recognition and development of particulate vaccines: does size matter? Methods 2006;40(1):1–9.

nature COMMUNICATIONS

ARTICLE

Received 24 Sep 2013 | Accepted 4 Mar 2014 | Published 10 Apr 2014

DOI: 10.1038/ncomms4566

Nucleic acid sensing by T cells initiates Th2 cell differentiation

Takayuki Imanishi[1], Chitose Ishihara[1], Mohamed El Sherif Gadelhaq Badr[1], Akiko Hashimoto-Tane[1], Yayoi Kimura[2], Taro Kawai[3,†], Osamu Takeuchi[3,†], Ken J. Ishii[4,5], Shun'ichiro Taniguchi[6], Tetsuo Noda[7], Hisashi Hirano[2], Frank Brombacher[8], Glen N. Barber[9], Shizuo Akira[3] & Takashi Saito[1,10]

While T-cell responses are directly modulated by Toll-like receptor (TLR) ligands, the mechanism and physiological function of nucleic acids (NAs)-mediated T cell costimulation remains unclear. Here we show that unlike in innate cells, T-cell costimulation is induced even by non-CpG DNA and by self-DNA, which is released from dead cells and complexes with antimicrobial peptides or histones. Such NA complexes are internalized by T cells and induce costimulatory responses independently of known NA sensors, including TLRs, RIG-I-like receptors (RLRs), inflammasomes and STING-dependent cytosolic DNA sensors. Such NA-mediated costimulation crucially induces Th2 differentiation by suppressing T-bet expression, followed by the induction of GATA-3 and Th2 cytokines. These findings unveil the function of NA sensing by T cells to trigger and amplify allergic inflammation.

[1] Laboratory for Cell Signaling, RCAI, RIKEN Center for Integrative Medical Sciences (IMS-RCAI), Yokohama, Kanagawa 230-0045, Japan. [2] Graduate School of Medical Life Sciences, Yokohama City University, Yokohama, Kanagawa 236-0004, Japan. [3] Laboratory of Host Defense, WPI Immunology Frontier Research Center, Osaka University, Suita, Osaka 565-0871, Japan. [4] Laboratory of Adjuvant Innovation, National Institute of Biomedical Innovation, Ibaraki, Osaka 567-0085, Japan. [5] Laboratories of Vaccine Science, WPI Immunology Frontier Research, Osaka University, Suita, Osaka 565-0871, Japan. [6] Department of Molecular Oncology, Institute of Pathogenesis and Disease Prevention, Shinshu University Graduate School of Medicine, Matsumoto, Nagano 390-8621, Japan. [7] Department of Cell Biology, Cancer Research Institute of the Japanese Foundation of Cancer Research, Toshima-ku, Tokyo 170-8455, Japan. [8] International Center for Genetic Engineering and Biotechnology, Cape Town Component and Institute of Infectious Diseases and Molecular Medicine, Faculty of Health Science, Division of Immunology, University of Cape Town, Cape Town, South Africa. [9] Department of Cell Biology and the Sylvester Comprehensive Cancer Center, University of Miami Miller School of Medicine, Miami, Florida 33136, USA. [10] Laboratory for Cell Signaling, WPI Immunology Frontier Research Center, Osaka University, Suita, Osaka 565-0871, Japan. † Present addresses: Laboratory of Molecular Immunobiology, Graduate School of Biological Sciences, Nara Institute of Science and Technology (NAIST), Ikoma, Nara 630-0192, Japan (T.K.); Laboratory of Infection and Prevention, Institute for Virus Research, Kyoto University, Sakyo-ku, Kyoto 606-8507, Japan (O.T.). Correspondence and requests for materials should be addressed to T.S. (email: saito@rcai.riken.jp).

Toll-like receptors (TLRs) sense pathogen-associated molecular patterns to initiate not only innate responses but also to help regulate T cell-mediated adaptive immune responses[1,2]. While some TLRs are expressed on the cell surface, NA-sensing TLRs such as TLR3, TLR7/8 and TLR9 are expressed in endosomal compartments, allowing specific recognition of endocytosed pathogens.

Recent studies have shown that T cells also express TLRs and that TLR ligands can directly modulate T-cell responses. For example, TLR2 ligands directly promote proliferation of activated T cells[3,4], modulate the proliferation and suppressive functions of $CD4^+CD25^+$ regulatory T cells[5,6], trigger Th1 effector functions independently of TCR stimulation[7] and modulate Th17 responses[8].

In addition, it has been reported that ligands for NA-sensing TLRs enhance IL-2 production and proliferation of anti-CD3 antibody (Ab)-stimulated T cells[9,10] and promote survival of activated T cells[11], and further that the TLR8 ligand inhibits the suppressive function of regulatory T cells[12]. However, except for TLR2, very little is known about the molecular basis of the NA-sensing mechanisms and the functional consequences of NA-mediated costimulation in T cells.

Naive $CD4^+$ T cells differentiate into various effector T helper (Th) cells such as Th1, Th2 and Th17 cells, which produce IFN-γ, IL-4/IL-5/IL-9/IL-13 and IL-17/IL-22, respectively[13]. While Th1 and Th17 cells exhibit protective functions against intracellular pathogens and extracellular bacteria/fungi, Th2 cells protect from helminthic infection. Contrary to these protective functions, the same Th subsets can play a role in disease pathogenesis: Th1 for inflammatory diseases, Th2 for allergic diseases and Th17 for autoimmune diseases. While TLR stimulation of antigen-presenting cells (APCs) results in the production of IL-12, which induces Th1 differentiation, Th2 development is induced by IL-4, but the cells responsible for the initial wave of IL-4 production needed to induce Th2 differentiation remain elusive[14].

In this study, we report that NA-induced costimulatory responses of $CD4^+$ T cells are mediated independently of known NA sensors in innate immunity. We found that T cells take up NAs to induce costimulation and that the NA-mediated costimulation requires higher-order structure of the NAs by forming complexes with the antimicrobial peptides or with core histones. More importantly, costimulation of naive $CD4^+$ T cell with NAs induces Th2 differentiation through the downregulation of T-bet and the upregulation of GATA-3 expression. Thus, NAs directly induce T-cell costimulation through a unique NA-sensing mechanism to trigger the initial IL-4 production for Th2 differentiation, which might be involved in triggering and amplification of allergic inflammation.

Results

TLR-independent NA-mediated costimulation of $CD4^+$ T cells. To elucidate the functional significance of NA stimulation, naive $CD4^+$ T cells were stimulated with each TLR ligand. While none of the TLR ligands alone were able to induce cell proliferation or IL-2 production, proliferation and IL-2 production were selectively enhanced by Pam3 (TLR1/2), MALP-2 (TLR2/6), poly(I:C) (TLR3) and CpG-B (TLR9) with anti-CD3 stimulation (Fig. 1a).

We next determined whether this response is mediated by TLRs using mice deficient in both MyD88 and TRIF, which lack the capacity to respond to any of the known TLR ligands. Surprisingly, both poly(I:C) and CpG-B-mediated costimulation were normal in the MyD88/TRIF-doubly deficient $CD4^+$ T cells, whereas MALP-2 (TLR2)-mediated costimulation was completely abrogated (Fig. 1b), demonstrating that poly(I:C) and CpG-B-mediated T-cell costimulation was induced independently of TLR signaling.

Notably, DNA lacking CpG motifs required for TLR9 activation, such as non-CpG oligodeoxynucleotide (ODN) and DNA encoding GFP (GFP-S and GFP-AS, antisense strand) could also induce costimulation for IL-2 production (Fig. 1c). These data indicate that DNA induces T-cell costimulation independently of the CpG motifs. We also found that poly(dA), poly(dC) and poly(dG) but not poly(dT) induced the costimulation for IL-2 production, although the uptake of poly(dT) and non-CpG ODN by T cells was comparable (Fig. 1d).

Confocal microscopy analysis revealed that non-CpG ODN colocalized with an endosomal marker dextran and a lysosomal marker LysoTracker (Fig. 1e), indicating that non-CpG ODN is taken up by T cells and transported to endosomes/lysosomes, similarly in innate cells, and induces costimulatory signals in a TLR-independent manner.

Higher-order structure of NA induces T-cell costimulation. It is noteworthy that CpG-A possessing a poly(dG)-tail induced stronger costimulation of $CD4^+$ T cells than other ODNs such as CpG-B and non-CpG (Fig. 1c). The importance of the poly(dG) tract was confirmed by the finding that control ODN GpC corresponding to CpG-A induces robust IL-2 production, similar to CpG-A (Fig. 2a), and that replacement of the poly(dG) motif of GpC by poly(dA), poly(dC) or poly(dT) resulted in the complete loss of stimulatory activity (Fig. 2b).

It has been reported that the poly(dG) tail induces the spontaneous formation of large multimeric aggregates via G-quadruplex formation[15]. Indeed, when GpC was rendered single-stranded by heating and flash-cooling, a dramatic reduction of IL-2 production was observed (Fig. 2c), suggesting that higher-order structures mediated by the poly(dG) motif are critical for enhanced costimulation by CpG-A and GpC. Consistently, introduction of a poly(dG)-tail to non-CpG and CpG-B that possess a phosphodiester (PO) backbone sensitive to DNase enabled them to induce costimulation, whereas the same DNA without the poly(dG)-tail could not (Fig. 2d).

It has been shown that the poly(dG) motif not only protects against DNase degradation[16] but also enhances the cellular uptake of the ODN[17]. Indeed, the uptake of GpC-poly(dC) by T cells was lower than GpC, indicating that GpC-poly(dC) could not induce costimulation due to its poor uptake (Fig. 2e). It is noteworthy that cellular uptake of GpC-poly(dC) was weaker than that of non-CpG (Fig. 2e). It has been reported that phosphorothioate (PS)-modified ODN are taken up more efficiently than PO-ODN[17]. The entire backbone of non-CpG is PS, whereas it is only partial in GpC (Supplementary Table 1). PS modification of GpC-poly(dC) led to enhanced cellular uptake and costimulation (Fig. 2e). By contrast, modification of non-CpG to contain only partial PS resulted in decreased uptake and the failure of costimulation (Fig. 2e). We also confirmed that cellular uptake and costimulation of PO-backboned non-CpG was much weaker than those of PS-backboned non-CpG (Supplementary Fig. 1a). These data indicate that efficient uptake of DNA via its poly(dG) tail or PS modification is critical for induction of costimulation.

While inosine or guanine-containing RNA such as poly(I), poly(G), poly(I:C) and poly(C:G) could induce costimulation, poly(A), poly(U), poly(C) and poly(A:U) could not (Fig. 2f). The induction of costimulation by RNA was correlated with the cellular uptake of RNA (Fig. 2f). These data indicate that RNA-mediated costimulation depends on the RNA sequence for cellular uptake of RNA to induce costimulation.